

**A MULTISCALE MODEL FOR BREAST-CONSERVATIVE
THERAPY: COMPUTATIONAL FRAMEWORK AND CLINICAL
VALIDATION**

A Thesis
Presented to
the Faculty of the Department of Computer Science
University of Houston

In Partial Fulfillment
of the Requirements for the Degree
Master of Science

By
Valentina Simonetti
August 2015

**A MULTISCALE MODEL FOR BREAST-CONSERVATIVE
THERAPY: COMPUTATIONAL FRAMEWORK AND CLINICAL
VALIDATION**

Valentina Simonetti

APPROVED:

Dr. Marc Garbey, chairman
dept. of Computer Science
University of Houston

Dr. Barbara L. Bass
dept. of Surgery
The Methodist Hospital Research Institute

Dr. Nikolaos V. Tsekos
dept. of Computer Science
University of Houston

Dean, College of Natural Sciences and Mathematics

Acknowledgements

I would like to thank my advisor Dr. Marc Garbey for his expertise and imperishable enthusiasm, and my tutor and friend Dr. Remi Salmon for his constant help and patience. I would like also to thank my Italian advisor Dr. Giuseppe Baselli and the ATLANTIS program, that gave me the unique opportunity to study in the USA and work for this project. I would like to express my gratitude to all the members of the committee for their help and support, in particular to Dr. Barbara L. Bass, without which this work would not be possible. I thank all my colleagues and friend from the laboratory, the hospital and the university for their concrete and psychological daily support. I thank also my family, my boyfriend, and my friends who are on the other side of the Atlantic; they were able to sustain me in all the difficulties I had to face, despite time and distance.

**A MULTISCALE MODEL FOR BREAST-CONSERVATIVE
THERAPY: COMPUTATIONAL FRAMEWORK AND CLINICAL
VALIDATION**

An Abstract of a Thesis
Presented to
the Faculty of the Department of Computer Science
University of Houston

In Partial Fulfillment
of the Requirements for the Degree
Master of Science

By
Valentina Simonetti
August 2015

Abstract

Breast cancer is the most common cancer among women worldwide and affects 12% of all the women in the USA. There exist different surgical approaches in order to defeat this kind of cancer: the traditional mastectomy (Breast Removal Surgery) and the more recent Breast-Conservative Therapy (BCT), whose goal is to preserve the breast contour and ameliorate the psychological impact of surgery on the patients. This work aims to exploit the BCT field developing a 3D patient-specific multiscale model that could predict the breast shape after lumpectomy, from surgery to complete healing. This model consists of two parts: a hyperelastic Neo-Hookean Finite-Element Model of the breast tissues and skin, and a Cellular Automata model that mimics the biology of healing after surgery. The resulting multiscale model shows results that agree with our theoretical assumptions and gives as outcome the breast contour after surgery depending on the anatomy of the patient and the input from the surgeon. This work is, in fact, the result of an interdisciplinary collaboration between surgeons, mathematicians and computer scientists. A clinical protocol that involves patients eligible for BCT was developed in order to validate this multiscale model with clinical data. The results obtained show the performance of the model and our findings based on the data of the first patient who took part of the study. The model validation gave us an error of maximum 2.5 cm for the surface comparison, which implies the need of further improvements. The Cellular Automata model showed fairly accurate results with the preliminary data, but we need more patients in order to obtain conclusions that are statistically consistent.

Contents

| | | |
|----------|---|-----------|
| 1 | Introduction and motivation | 1 |
| 1.1 | Breast anatomy and breast cancer | 1 |
| 1.2 | Surgical approaches to breast cancer | 3 |
| 1.3 | Biology of wound healing | 4 |
| 1.4 | Aim of the work | 7 |
| 2 | State of the art | 9 |
| 2.1 | Mechanical models | 9 |
| 2.2 | Healing models | 10 |
| 2.3 | Cellular automata | 11 |
| 2.4 | Breast 3D surface imaging | 12 |
| 3 | Methods and protocol | 13 |
| 3.1 | Mechanical model | 13 |
| 3.2 | CA model for wound healing | 15 |
| 3.3 | Validation of multiscale model | 27 |
| 3.3.1 | Clinical study | 27 |
| 3.3.2 | Surface acquisition and comparison | 30 |
| 4 | Results | 40 |
| 4.1 | Validation of 3D CA | 40 |
| 4.2 | Validation of the mechanical model | 44 |
| 4.3 | Rough validation in patient specific case | 45 |

| | |
|---|-----------|
| 5 Discussion and future developments | 51 |
| 5.1 Validation of the CA model | 51 |
| 5.2 Validation of the mechanical model | 52 |
| 5.3 Rough validation in patient specific case | 53 |
| 5.4 Future developments | 53 |
| Bibliography | 57 |

List of Figures

| | | |
|-----|---|----|
| 1.1 | Detailed breast anatomy. | 2 |
| 1.2 | Histological samples of breast tumor tissue in the three different grades. Left: low grade, center: intermediate grade, right: high grade | 3 |
| 1.3 | Different surgical approaches for breast cancer. On the left: mastectomy. On the right: lumpectomy | 4 |
| 1.4 | Wound-healing process as described in [37] | 6 |
| 1.5 | Scheme that shows how the multiscale model works: the mechanical model reconstructs the breast shape under gravity, computes the stress distribution around the cavity left by lumpectomy, and sends it to the CA model of wound healing. The CA model uses the stress values in every point of the space in order to set specific parameters, and gives back the shape of the cavity. This process is repeated for different time steps till the complete closure of the cavity. | 8 |
| 3.1 | MRI of the breast on transverse, sagittal, and coronal plane, where the tumor was located manually by the surgeon (red circles). | 14 |
| 3.2 | Result of the breast reconstruction from MRI. The initial mesh is with zero gravity, then we apply the acceleration vector to obtain the shape under gravity. | 15 |
| 3.3 | Hexagonal closed-packed geometry | 16 |
| 3.4 | Wound healing cycle where we can see the main stages of the CA model (inside the dotted line) and the data it receives and sends to the mechanical model. The mechanical model generates a 3D map of strain energy values around the area of the cavity (on the top right) and sends it to the CA model, whereas the CA model sends back to the mechanical model the new coordinates of the points of the cavity after one time step of the healing process. This process keeps repeating till the 3D matrix that contains the coordinates of the points of the cavity is empty | 19 |
| 3.5 | Left: hexagonal close-packed grid, which represent the domain. Right: points of wound cavity after virtual lumpectomy. Both the graphs are in arbitrary units (a.u.). | 20 |
| 3.6 | Wound edge (red) with cells selected for division (black) | 21 |

| | | |
|------|--|----|
| 3.7 | Probability map result of the application of the diffusion algorithm on one cell positioned in the center of the hcp grid, with $\lambda = 0.5$ and $N_d = 60$. View of one plane. | 23 |
| 3.8 | Example of normalized strain distribution around the wound area, where 0 is the center of the cavity and the values of the axis are in mm | 25 |
| 3.9 | Study design | 28 |
| 3.10 | Left: LOGIQ e machine. Right: 12L-RS linear probe by GE | 29 |
| 3.11 | From the top: ellipsoid that represents the cavity shape and two US acquisitions of the same cavity with probe orientation at the moment of the acquisition | 30 |
| 3.12 | Top: Kinect device from Microsoft. Bottom: Kinect components | 32 |
| 3.13 | Top: Refusion graphic user interface at the moment of the volume acquisition. Bottom: Refusion graphic user interface after the volume acquisition and reconstruction | 33 |
| 3.14 | Camera calibrator user interface where we can see: on the left, the list of pictures used to feed the algorithm of calibration, in the center, the result of the chessboard detection, and on the right, the histogram of the mean error for each image and its extrinsic parameters (position of the camera in respect to the chessboard origin which is the top left corner of the chessboard itself). | 34 |
| 3.15 | Phantom profile and tilting angles of the camera using the nipple as center of rotation | 35 |
| 3.16 | Support for kinect that allows a rotational movement around the patient breast at the moment of the surface acquisition. | 36 |
| 3.17 | Process of orientation of the cloud point. (a) Reference selection on the cloud point using regular box at the moment of acquisition. (b) Orientation of the cloud point using the nipple as center of rotation and the tilting angles retrieved from the calibration process. | 38 |
| 3.18 | Comparison of the 2 profiles | 39 |
| 3.19 | errors: left static, right with breathing simulation | 39 |
| 3.20 | CloudCompare workspace where we loaded the result of the 3D-SI of breast | 39 |
| 4.1 | Evolution of wound closing in stress free conditions for the three perpendicular planes that pass by the center of the volume. From top to bottom: initial condition, after 30 time steps and after 85 time steps. | 41 |
| 4.2 | a) Diameter (in units) of the cavity for the three different axis passing by the center of the cavity where we can see how the three axis have the same behavior. b) displacement of the center of the cavity from the initial position, where we can see that the center of the cavity does not move consistently from the initial position during the healing process. | 42 |

| | | |
|------|---|----|
| 4.3 | Evolution of wound closing for the three perpendicular planes with maximum stress value for the lower half of the volume and zero for the rest. From top to bottom: after 5 time steps, after 20 time steps and after 55 time steps | 43 |
| 4.4 | (a) Diameters (in units) of the cavity for the three different axis passing by the center of the volume where we can see how the three axis lost the symmetric behavior. (b) Diameters of the cavity for the three different axis passing by the center of the cavity, that changes coordinates for every iteration, as shown in (c) .(c) Displacement of the center of the cavity from the initial position. | 44 |
| 4.5 | Results of the comparison between pre-operative 3D-SI and outcome of mechanical model without lumpectomy. The figure shows different views of the breast where the color of each point represents the value of distance (signed) between the model and the reference in cm. | 45 |
| 4.6 | Sagittal view of the breast reconstructed from MRI data where we performed a virtual lumpectomy with same characteristics of the patient-specific case, and where then we applied gravity. | 46 |
| 4.7 | (a) Initialization of the mechanical model. (b) Result after 30 time steps. (c) Result after 50 time steps. | 48 |
| 4.8 | Evolution of wound closing from the simulation initialized with real data obtained from the first patient. View for the three perpendicular planes that pass by the center of the volume. From top to bottom: initial condition, after 30 time steps and after 50 time steps | 49 |
| 4.9 | (a) Diameters (in units) of the cavity initialized with real values, for the three different axis passing by the center of the volume. (b) Displacement of the center of the cavity from the initial position. | 50 |
| 4.10 | Maximum strain energy values (in Joules) during the closing process in two conditions: cell mitosis depends on strain energy (blue), cell mitosis not driven by strain energy (red) | 50 |
| 5.1 | (a) User interface of the “Virtual Lumpectomy” software, where the user can load the MRI data from the patient files, select the center of the lumpectomy, the radius, and the healing speed. (b) Outcome of the simulation, where the user can see the result of the virtual surgery during the healing process, and obtain an approximation of the time of healing. | 56 |

List of Tables

4.1 Volume estimation of the cavity during time 46

Chapter 1

Introduction and motivation

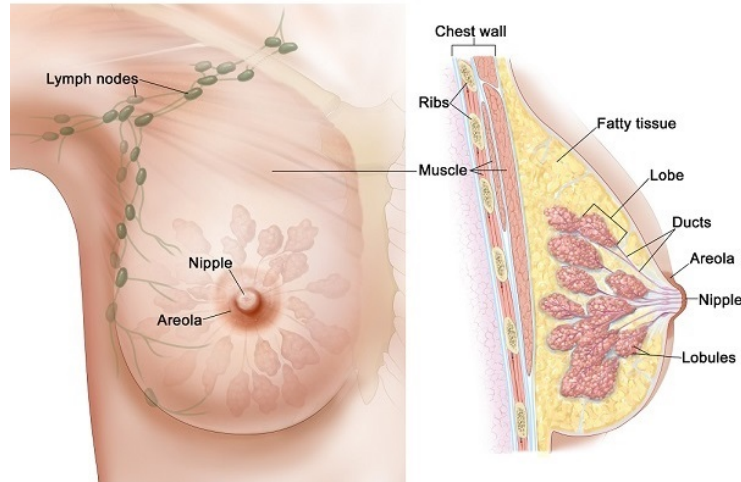
Breast cancer is the most common cancer in women worldwide [23] and affects around the 12% of the U.S. women over the course of their lifetime [51].

Significant improvements have been made in terms of early detection of this cancer during the last years; as a results of this, fields like Breast Conservative Therapy (BCT) gained a crucial importance in order to minimize the physical and psychological impact of surgery on the patient. With this work we want to exploit this field implementing a model for breast that underwent lumpectomy and, in this way, offer a powerful and reliable tool able to predict the outcome of the surgery and improve the process of surgery planning in order to achieve the best possible aesthetic result. Currently there is nothing able to play this role and all the decisions rely only on the surgeon's experience.

1.1 Breast anatomy and breast cancer

Female breast is made of a collection of fat cells called adipose tissue, lobes composed by lobules (small glands that produce milk), and milk ducts. Along with adipose tissue, there is a network of ligaments, connective tissue, nerves, lymph vessels, lymph nodes, and blood vessels (Figure 1.1).

Figure 1.1: Detailed breast anatomy.



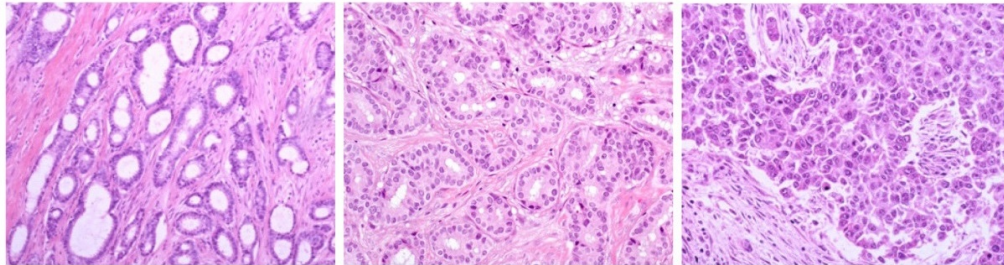
Due to genetic and environmental effects, some breast cells can become abnormal, leading to aggressive cell growth and formation of a tumor. Whether this tumor is malignant it gets cancerous and can affect surrounding cells, spreading inside healthy tissue. Breast cancer usually begins in the lobules (Lobular Carcinoma) or in the milk ducts (Ductal Carcinoma) and can be diagnosed as invasive (spread in surrounding tissue) or in-situ (localized in the area where it originated) [21].

Basing on the severity of mutation, malignant tumors are classified in three different grades considering how much cancer cells look like normal cells [30] (Figure 1.2):

- Low-grade, or well differentiated
- Intermediate-grade, or moderately differentiated
- High-grade, or poorly differentiated

Breast cancers differentiate also in terms of cancer stages [51]. Stage is usually expressed in a scale that goes from 0 through IV, with stage 0 describing localized non-invasive cancers, and stage IV describing invasive cancers that have spread to other parts of the body. Cancer stage is determined considering four main factors:

Figure 1.2: Histological samples of breast tumor tissue in the three different grades. Left: low grade, center: intermediate grade, right: high grade



- Size of the cancer
- Whether the cancer is invasive or not
- Whether the cancer is in the lymph nodes
- Whether the cancer has spread to other parts of the body

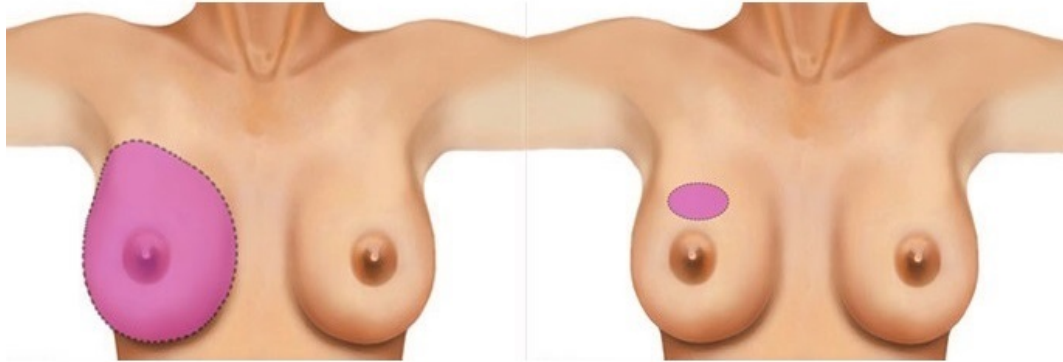
1.2 Surgical approaches to breast cancer

Surgical approaches to breast cancer are of two types:

- Mastectomy (breast removing surgery): complete removal of the breast (Figure 1.3 on the left).
- Lumpectomy (breast conservative surgery): removal of the tumor mass (lump), as well as rim of normal tissue around it (margins) (Figure 1.3 on the right).

Mastectomy is the most traditional approach and can be performed for any stage of breast cancer, whereas lumpectomy can be performed just in case of lower stages cancer (stage I or stage II). BCT consists of lumpectomy followed by moderate-dose radiation therapy in order to eliminate any possible microscopic residual trace of abnormal cells. BCT allows the woman to preserve her

Figure 1.3: Different surgical approaches for breast cancer. On the left: mastectomy. On the right: lumpectomy



breast and obtain an aesthetic outcome closer to the pre-operative one without the need of any kind of prosthesis; however, sometimes, this surgery can result as asymmetry and deformities [8]. Most of the time, patients require total mastectomy thinking that the complete removal of the breast mass would avoid definitively the risk of cancer recurrence, but mastectomy does not guarantee complete lack of local recurrence. Different statistical studies regarding surgical approaches for early-stage tumors tried to evaluate whether there are significant differences between mastectomy and BCT [46][14][6][62][1][5]: BCT showed same or even better results in terms of survival rates and local recurrence of the tumor. Considering this evaluation, BCT is a really valuable alternative for breast surgery that does not involve additional risk for survival and allows to obtain better cosmetic aspect along with a better quality of life for the patient after surgery. At the moment just surgical experience can try to predict the specific aesthetic impact of lumpectomy on the breast.

1.3 Biology of wound healing

Closure of wound in adults depends on cell mitosis and migration of cells, which led to the thickening and restoration of tissue.

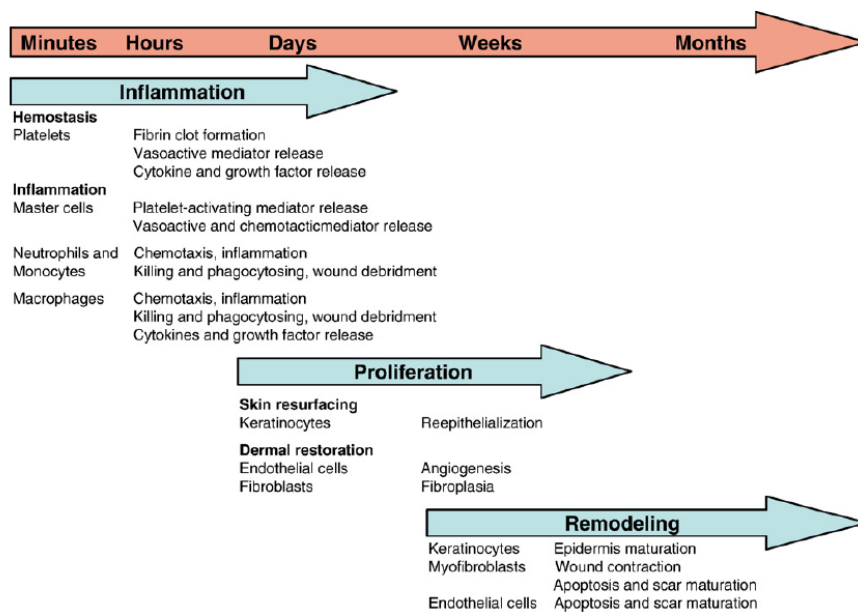
The process of closing of the cavity left by lumpectomy follows all the phases of acute wound

healing, which are [37] (Figure 1.4):

- **Inflammatory phase:** as consequences of the tissue damage, we have vascular and cellular responses: local vasodilatation and fluid extravasation in extravascular space produce signs of inflammation like swelling, redness, and heat. This condition usually lasts between 24 and 48 hours. Homeostasis plays a fundamental role during this first stage: platelets led to blood coagulation and start the healing cascade releasing chemical mediators and growth factors including transforming growth factor (TGF- α , TGF- β) and platelet-derived growth factor (PDGF); growth factors stimulate cell proliferation, angiogenesis, and extracellular matrix synthesis. Platelets also work as scaffolds for cell recruitment inside the cavity: neutrophils and macrophages spread from capillaries inside the cavity and remove tissues debris and bacteria.
- **Proliferative phase:** the major events of this phase are reepithelialization, angiogenesis (creation of new vessels for blood supply) and fibroplasia (reinforcement of damaged tissue). Reepithelialization is the process of formation of a new protective layer of epidermis that protects the damaged tissue below. Fibroplasia is the process of fibroblast proliferation, creation of fibrin clot, and production of collagen and proteins, which contribute to the formation of granulation tissue. Fibroblast proliferation is influenced by growth factors and low oxygen condition. Angiogenesis is the growing and spreading of new vessels inside the wound from adjacent preexisting vessels; the development of new capillary vessels depends on cells and kitochines present, and on the structure of the extracellular matrix that acts as scaffold support. Another significant process that takes place during this phase is wound contraction: this reduction of wound size is mediated by myofibroblast and starts producing effects around the second week after wound formation.
- **Remodeling phase:** this phase can last up to two years. The extracellular matrix composition changes and collagen plays a key role in it. Collagen constitutes the 80% of normal human dermis and provides structure, strength, and stiffness to dermal tissue. In normal conditions for adults, 80% of this collagen is type I collagen, whereas the 10% is type III collagen.

During early acute wound healing, type III collagen is the predominant type synthesized by fibroblasts in granulation tissue (maximal secretion around 5 and 7 days). The maximum amount of collagen is reached between the second and the third week after injury. After a period of one year or longer the tissue returns back to its normal composition (mainly type I collagen), reaching up to 70% pre-injury strength.

Figure 1.4: Wound-healing process as described in [37]



Understanding the processes involved in healing process is crucial in order to organize patient-specific therapies that could shorten the time for functional recovery and prevent or reduce aesthetic effects on tissues.

Mathematical modeling and computer simulation play a fundamental role in this field.

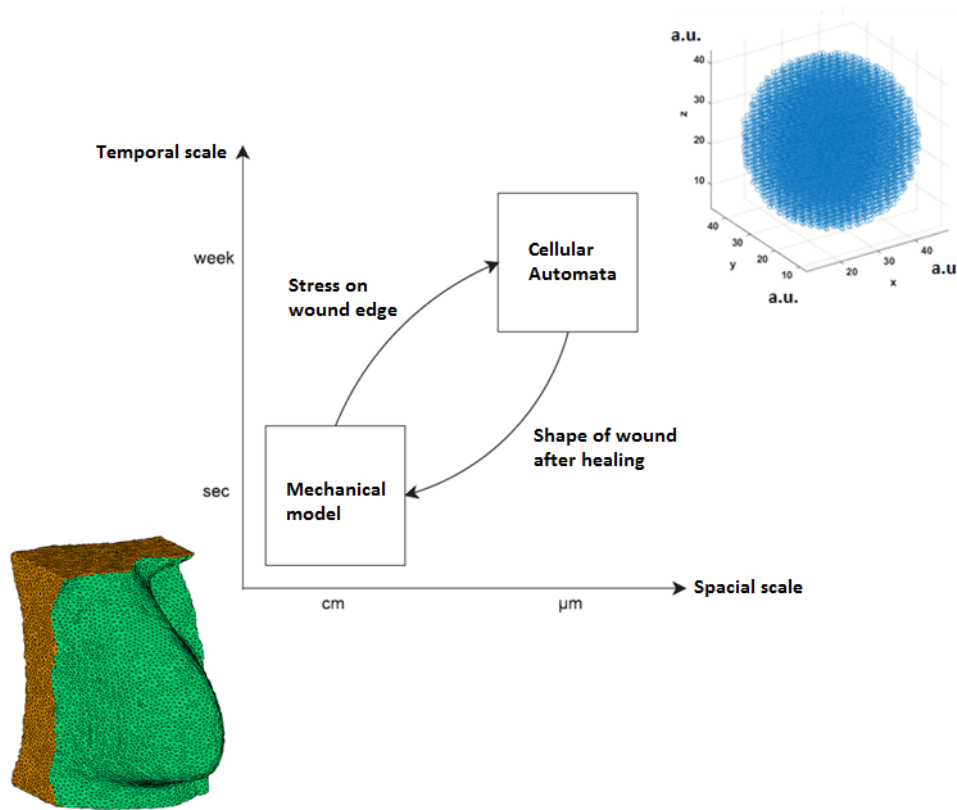
1.4 Aim of the work

The aim of this work is to create a more-complete, flexible, and realistic version of a previous multiscale model [22]. The previous model provides a long-time-scale prediction of breast shape after tumor resection coupling 2D models for mechanic and biology, and taking into account just the sagittal plane of the breast passing through the nipple assuming symmetry. The validation was performed on one patient who underwent lumpectomy with a tumor positioned above the nipple exactly on the sagittal plane passing through the nipple.

Along with the computational framework of a 3D Neo-Hookean Finite-Element (FE) model that takes care of the mechanic of breast, we implemented a 3D Cellular Automata (CA) biological model that mimics the biology of wound healing in order to simulate the closing of the cavity left by lumpectomy: the resulting 3D multiscale model (Figure 1.5) has the aim of giving an approximate prediction of the 3D surface of the breast after surgery without limitations regarding the tumor position. The mechanical model is initialized using pre-operative MRI images of the patient, whereas the biological model is initialized with a sphere that has the dimension of the tumor mass.

As the result of a collaboration between mathematics, computer scientists and surgeons, this work proposes also a clinical protocol for 3D validation of the general case and shows the results obtained from a pilot study with a woman who has been selected to undergo BCT and has been treated in Houston Methodist hospital.

Figure 1.5: Scheme that shows how the multiscale model works: the mechanical model reconstructs the breast shape under gravity, computes the stress distribution around the cavity left by lumpectomy, and sends it to the CA model of wound healing. The CA model uses the stress values in every point of the space in order to set specific parameters, and gives back the shape of the cavity. This process is repeated for different time steps till the complete closure of the cavity.



Chapter 2

State of the art

2.1 Mechanical models

Breast modeling consists of modeling adipose and glandular tissue, along with modeling the skin that surrounds it. In both cases we have to describe soft-tissue deformations, which are non-rigid and, thus, cannot be modeled with rigid transformations. FE methods, in particular hyperelastic Neo-Hookean methods, resulted particularly effective in modeling large deformations of soft tissue like breast tissue [11][18][13] [17][55][57]. The problem of building a mechanical model of the breast can be decomposed in two sub-problems: create a mechanical model for adipose and glandular tissue, and create a model for the skin envelope. Skin plays an important role in determining the breast shape under gravity and its behavior is highly nonlinear, anisotropic, and viscoelastic [64][33][19]. Due to its characteristics, skin can be modeled using triangular or quadrilateral surface elements [57] [17]. Hyperelastic models, such as neo-Hookean models, also appear effective in modeling the skin behavior [25][36].

2.2 Healing models

Understanding and modeling the complex process of wound healing can be a powerful tool for optimization of surgery planning and recovery. The healing process is driven by so many different factors that is almost impossible to try to model the combined effect of all of them, considering also that is virtually impossible to modulate each one of them in order to evaluate its effect during the healing process. The literature offers different kind of approaches [70], in terms of modeling, that go from differential equation-based and agent-based models to tissue realistic and hybrid models.

Differential equation-based models

Modeling biological processes as wound healing using differential equations is probably the most standard and classical way. There are three classes of equation-based models: models based on ordinary differential equations (ODEs), models based on partial differential equations (PDEs), and models based on the level-set method [52]. ODEs can describe the time dependence of the wound-healing process but not its spatial variability, whereas PDEs and level set can describe both. Differential equation-based models have been used in order to describe all the principal phases of wound-healing [3][16][43], from inflammation [63], to proliferation [4], and remodeling [42]. Equation-based models are really important for a mechanistic point of view and also to have an insight into biological processes and their dynamics. On the other hand, these models are not suited for tissue-realistic simulations that are driven also by stochastic biological effects.

Agent-based models

Agent-based models (ABM) are discrete rule-based models which are well suited for spatial and stochastic effect at cellular level. Agents of the models are the computational units (cells, molecules...) which are driven by rules that are discrete approximation of real continuous biological phenomena [2]. These rules define local instantaneous interactions between the units and can include probabilistic components that determine stochastic biologic effects over the final outcome of the system

as a whole. Due to their nature, ABM seem well suited for modeling wound healing and create a link between basic medical knowledge and clinical strategies [20].

Hybrid models

Hybrid modeling is the result of a recent approach that involves the combination of different computational models into a single simulation [40][69], like in [59], where ODE were used to define certain agent rules (low-level details), and ABM to describe the behavior of the high-level components of the system.

2.3 Cellular automata

CA are discrete and local dynamic systems [66], introduced for the first time around 1950 by Stanislas Ulam, John von Neumann, and Konrad Zuse.

CA are specific ABM with these characteristics [65]:

- Regular arrangement of cells of the same kind
- Each cell has a finite number of states
- Cell states are updated simultaneously at discrete time levels
- Rules are deterministic and uniform in space and time
- Rules for one cell depend on its state and also on the local neighborhood of the cell itself

CA is a particular kind of ABM: each cell is a unit and undergoes specific rules designed for it. Whereas general ABM can be lattice-free [10][68], CA needs a lattice with well defined geometry [26][58][12]. CA models have been recently proposed in several biologic applications that deal with result of interaction between microscopic units, like cells [41][44][9].

2.4 Breast 3D surface imaging

“Three-dimensional (3D) imaging” refers to techniques, as Magnetic Resonance Imaging (MRI) and Computed Tomography (CT), that process true internal data acquiring voxels (volumetric pixels). On the other hand, the imaging process that measures and analyzes surfaces in 3D space is called “3D surface imaging” (3D-SI). 3D-SI has been really important during the last years in different clinical studies, leading to the development of different new technologies. A recent review of Tzou et al.[61] compared five of the current 3D-SI technologies on the market which are currently used in clinical environment: these systems can be divided in two groups that differ in terms of the surface acquisition methods used. This methods are of two types: structured light [50] and stereophotogrammetry. 3D-SI, along with the above-mentioned technologies, have been validated and used in the fields of aesthetic, oncoplastic, and breast surgery [67][34][39][38], in particular for BCT [47][28]. An extensive review about 3D-SI for breast surface assessment was made by O’Connell et al. in 2015 [49]. The systems most used now in the clinical field are expensive, heavy, and bulky, limiting the imaging process to a specific room. Some studies explored the possibilities of breast 3D-SI using smaller, more portable, and cost effective devices [29][54]. Particularly interesting for our study is a work by Henseler et al. of 2014 [27], that validates the performance of the the Kinect device from Microsoft [45] on three-dimensional estimated volume of different breast prostheses.

Chapter 3

Methods and protocol

As mentioned above, the result of this work is a 3D multiscale model of breast after lumpectomy, from surgery to complete healing. The complete 3D multiscale model consists of two parts: a Neo-Hookean FE mechanical model for the breast shape, and a biological CA model for wound healing. We are going to describe both of them with a better inside view of the biological CA model for wound healing.

3.1 Mechanical model

While the 3D CA model has been developed during this work, the mechanical model was developed in a previous study by Salmon et al.[56].

This mechanical model is a compressible, isotropic, Neo-Hookean hyperelastic model which is particularly suited for soft tissue deformation, such as breast tissue. The model is initialized with segmented and interpolated pre-operative MRI data of the patient where the tumor position was manually selected by the surgeon (Figure 3.1). Using a FE method, it can reconstruct 3D meshes of the patient breast that are made by tetrahedral elements for soft tissue and triangular elements for the skin (shell elements). The volume obtained is the breast shape with zero gravity. After this

process, the model mimics the mechanical effect of gravity on the tissue applying the acceleration vector on each point of the mesh (Figure 3.2). In order to obtain this result, it takes into account these boundary conditions:

- No displacement of chest wall
- No displacement of top and bottom section of skin.

Figure 3.1: MRI of the breast on transverse, sagittal, and coronal plane, where the tumor was located manually by the surgeon (red circles).

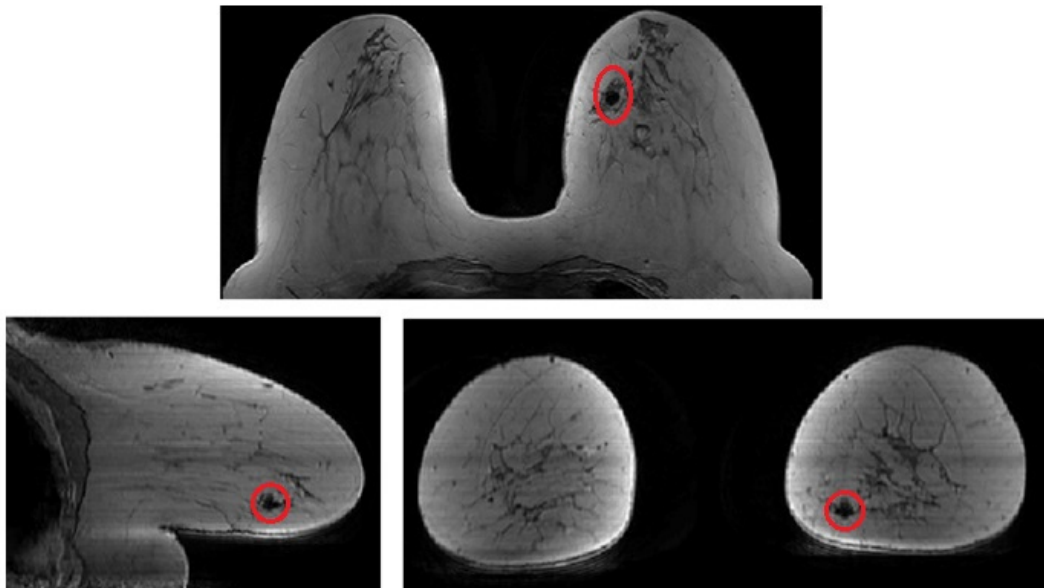
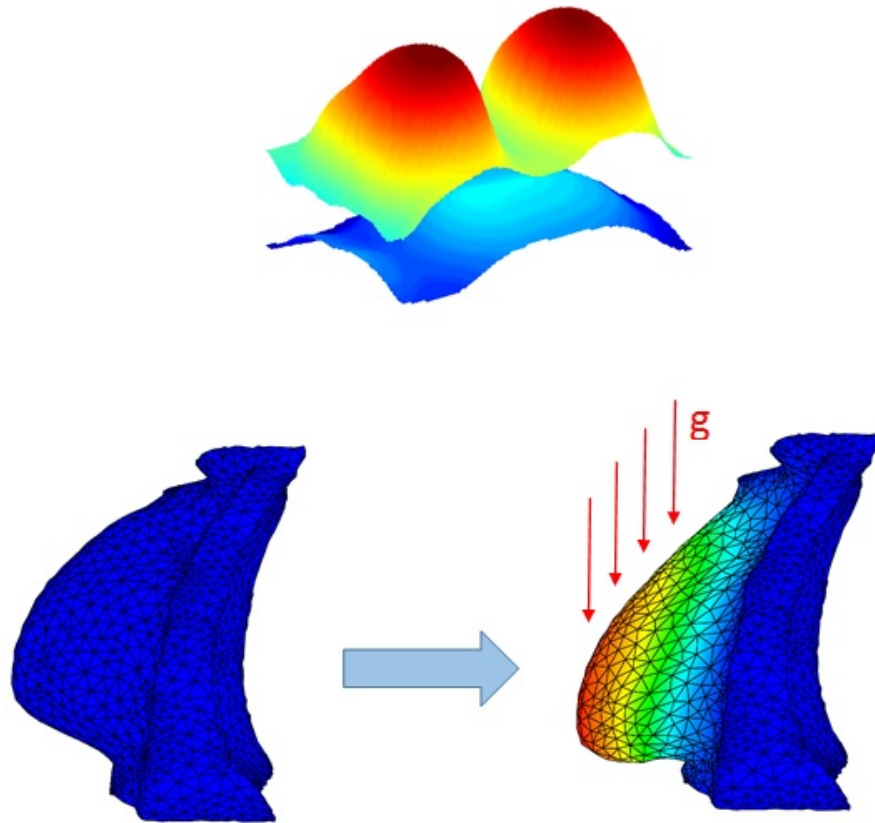


Figure 3.2: Result of the breast reconstruction from MRI. The initial mesh is with zero gravity, then we apply the acceleration vector to obtain the shape under gravity.

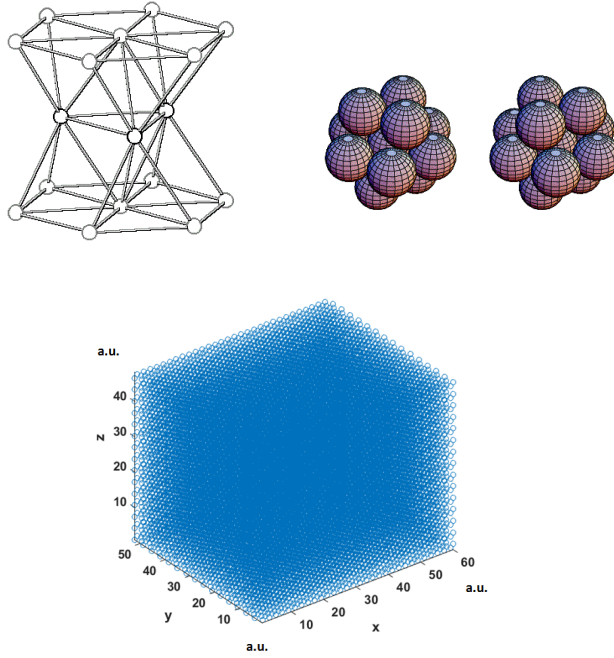


3.2 CA model for wound healing

The CA model for wound healing we present is implemented in Matlab and is a 3D evolution of the 2D model presented in [22]. We built a CA based on simplified biological rules that drive the complex process of healing. A lot of questions are still open regarding this approach, indeed the aim of this work is to obtain an initial phenomenological description that can be refined and validated by clinical data.

The CA is built on an hexagonal close-packed (hcp) lattice: this geometry allows the highest density that can be obtained by arrangement of equal spheres [24](Figure 3.3) and it can model the organization of cells in space. We could imagine it as the arrangement of cannonballs in a pile.

Figure 3.3: Hexagonal closed-packed geometry



The density of units is different for the three axis, indeed we can describe the position of all the sphere centers as:

$$\begin{bmatrix} 2i + ((j + k)\%2) \\ \sqrt{3}[j + \frac{1}{3}(k\%2)] \\ \frac{2\sqrt{6}}{3}k \end{bmatrix} r \quad (3.1)$$

That is the matrix containing the coordinates of all the spheres centers in space along x, y, and z direction, where:

r : radius of the unit sphere

%: modulo operator which, in this case, differentiates the cases where the line and the plane considered are odd or even

i, j, k : indices starting from 0 to the the length of x,y, and z coordinate

Each position has 12 neighbors: 6 on the same plane, three above, and three below. All the positions are equally spaced from the neighbors. Each site of the grid can be occupied by one cell or be free. Behavior of cells depends on probability laws which are function of the position of the cell and its neighbors, along with environmental conditions.

First environmental condition is the concentration of Tissue Growth Factor (TGF) near the wound edge transported by the diffusion operator. Following Javierre et al. [32], concentration of TGF follows the equation:

$$\frac{\partial c}{\partial t} - \nu \Delta c + \lambda c = \chi_{al} \quad (3.2)$$

Where:

c : concentration of TGF

ν : diffusion rate of TGF

λ : decay rate of TGF

χ_{al} : unit step function equal to 1 inside a layer of fixed width around the wound edge, referred to as an “active layer”, and 0 elsewhere

Second environmental condition is the mechanical strain energy acting around the wound edge [31]. The mechanical strain energy E is calculated like in [60] as the effective stress s_{eff} times the effective strain e_{eff} as in Equation 3.3.

$$E = s_{eff} \times e_{eff} \quad (3.3)$$

s_{eff} and e_{eff} are defined as:

$$s_{eff} = \frac{1}{2^{\frac{1}{2}}} \{(s_1 - s_2)^2 + (s_2 - s_3)^3 + (s_3 - s_1)^2\}^{\frac{1}{2}} \quad (3.4)$$

$$e_{eff} = \frac{2^{\frac{1}{2}}}{3} \{(e_1 - e_2)^2 + (e_2 - e_3)^3 + (e_3 - e_1)^2\}^{\frac{1}{2}} \quad (3.5)$$

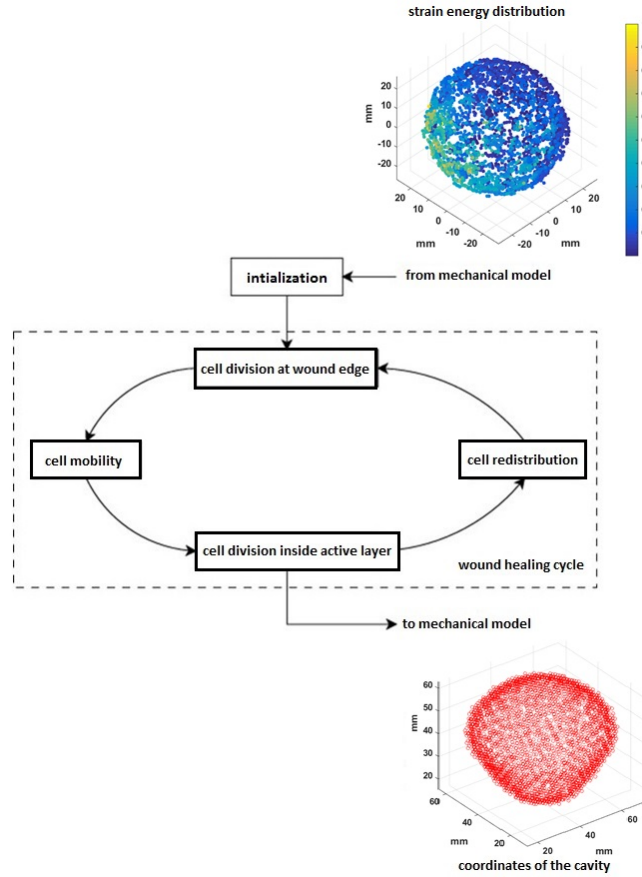
Where:

s_1, s_2, s_3 : principal stresses defined as the eigenvalues of the stress tensor

e_1, e_2, e_3 : principal strains defined as the eigenvalues of the strain tensor

The CA model obtains data and sends results to the mechanical model during all the virtual healing process in order to integrate biological data (from mitosis and redistribution) and mechanical data, in a loop that keeps running until the cavity is completely closed. For every iteration, the mechanical model computes the value of strain energy in every point of the area around the cavity and sends this 3D matrix to the biological model. The biological model interpolates this values of strain energy in order to fit the hcp lattice, then uses them to drive specific phenomena that influence the wound healing. A summary of the process is in Figure 3.4.

Figure 3.4: Wound healing cycle where we can see the main stages of the CA model (inside the dotted line) and the data it receives and sends to the mechanical model. The mechanical model generates a 3D map of strain energy values around the area of the cavity (on the top right) and sends it to the CA model, whereas the CA model sends back to the mechanical model the new coordinates of the points of the cavity after one time step of the healing process. This process keeps repeating till the 3D matrix that contains the coordinates of the points of the cavity is empty



We are going to describe in details all the processes modeled inside the CA model, but we need to introduce few notations:

Ω : computational domain, is a cube of dimensions $D_x \times D_y \times D_z$ (Figure 3.5, left)

Ω_{wound} : domain occupied by wound area (filled sphere), centered in Ω (Figure 3.5, right)

Γ : wound edge (empty sphere)

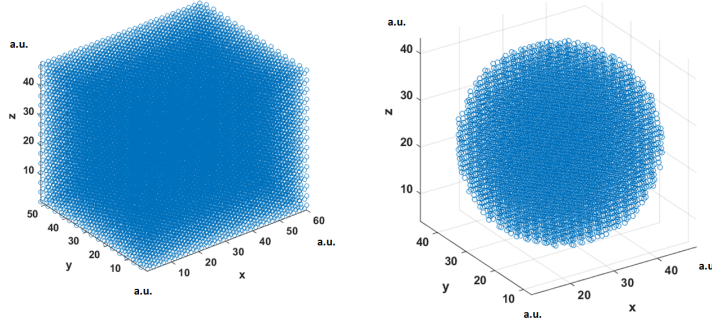
u_i : state variable of CA

$$u_i = \begin{cases} 0 & \text{no cell} \\ 1 & \text{cell} \end{cases}$$

Each site u_i has 12 neighbors $u_j, j \in M_i$.

The algorithm consists of four steps that we are going to describe in detail.

Figure 3.5: Left: hexagonal close-packed grid, which represent the domain. Right: points of wound cavity after virtual lumpectomy. Both the graphs are in arbitrary units (a.u.).



Cell division at wound edge

This part models the process of mitosis at the wound edge. Each cell which is part of the wound edge Γ has probability p_{edge} of undergoing through mitosis. For each cell of Γ we compute $n_i \in [0, 1]$, which is a randomly generated value from a uniform distribution. If the random probability results

lower than the limit, there is mitosis: the new cell will be randomly positioned in one of the 12 neighbor positions which are inside the wound area (Ω_{wound}). p_{edge} is a free parameter we set to 0.05 (5% probability of mitosis). Algorithm 3.1 describes this process in detail and in Figure 3.6 we can see the result of the random selection of cells from the edge of the cavity.

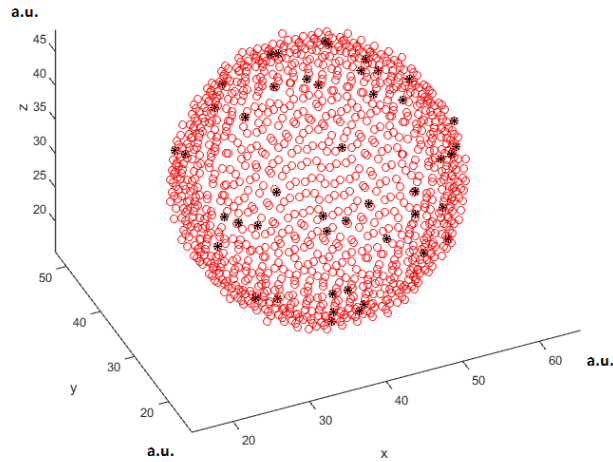
Algorithm 3.1 Cell division at wound edge

```

if  $u_i \in \Gamma$  and  $n_i < p_{edge}$  then
  choose randomly  $j$  such that  $u_j \in \Omega_{wound}$ ,  $j \in M_j$  and set  $u_j^{new} = 1$ 
end if

```

Figure 3.6: Wound edge (red) with cells selected for division (black)



Cell mobility

Cells of the edge can migrate randomly to every adjacent free site due to diffusion for Brownian motion. We can compute the probability distribution with the diffusion operator:

$$\partial_t - \Delta$$

In our case we have to compute the probability distribution $p_i \in [0, 1]$ of finding a cell in that location after a certain number of steps of diffusion; we used a P1 finite element approximation of the diffusion operator where the value of the specific site after one step depends on the value of the site the step before plus a function of the values of the 12 neighbors that surround it (Equation 3.6). The initialization is the CA state variable u_i that is 1 or 0.

$$p_i^{n+1} = p_i^n + \lambda \left(\frac{1}{12} \sum_{j \in M_i} p_j^n - p_i^n \right), \quad n = 0 \dots N_d - 1 \quad (3.6)$$

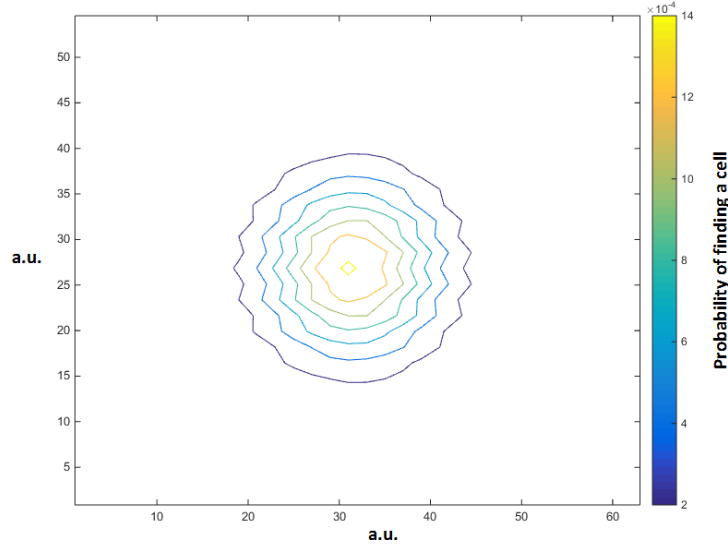
Where λ is the diffusion coefficient that we set with a value of 0.5.

N_d is the number of steps performed and is a free parameter that characterizes the motility of the cells.

Figure 3.7 shows how, applying this algorithm to a single cell positioned at the center of the grid, we have a circular shape for the probability levels of finding the cell in that position after a certain amount of time steps.

After the application of the diffusion algorithm, we obtain a 3D map of probability distribution where each site of the grid has a value $\in [0, 1]$. We need to preserve the total number of cells we have before diffusion, so we compute a level set with an algorithm that uses the number of cells as a stopping factor (Algorithm 3.2). The level set obtained is the new edge of the wound after cells redistribution. N_d , the number of time steps for the algorithm, is a free parameter.

Figure 3.7: Probability map result of the application of the diffusion algorithm on one cell positioned in the center of the hcp grid, with $\lambda = 0.5$ and $N_d = 60$. View of one plane.



Cell division inside active layer

As mentioned above, as considered in [32], we take into account the active layer, which is a thin strip of cells around the cavity where we have diffusion of TGF from the edge of the wound through the tissue, following:

$$\frac{\partial c}{\partial t} - \nu \Delta c + \lambda c = \chi_{al} \quad (3.7)$$

c : concentration of TGF

ν : diffusion rate of TGF

λ : decay rate of TGF

χ_{al} : unit step function equal to 1 inside a layer of fixed width around the wound edge, referred to as an “active layer”, and 0 elsewhere

Mitosis in the active layer is also influenced by local strain energy. In our case the local value for

Algorithm 3.2 Redistribution algorithm

```
tA = 0
tB = 1
while ∑ uinew ≠ ∑ uiinitial do
  U0 =  $\frac{1}{2}(t_A + t_B)$ 
  uinew =  $\begin{cases} 1 & \text{if } p_i \geq U_0 \\ 0 & \text{if } p_i < U_0 \end{cases}$ 
  if ∑ uinew > ∑ uiinitial then
    tA = U0
  else
    tB = U0
  end if
end while
```

strain energy is obtained from the mechanical model as shown in Figure 1.4, and results as a 3D matrix of normalized energy values between 0 and 1 (Figure 3.8).

The final equation that drives the probability of mitosis in the active layer is:

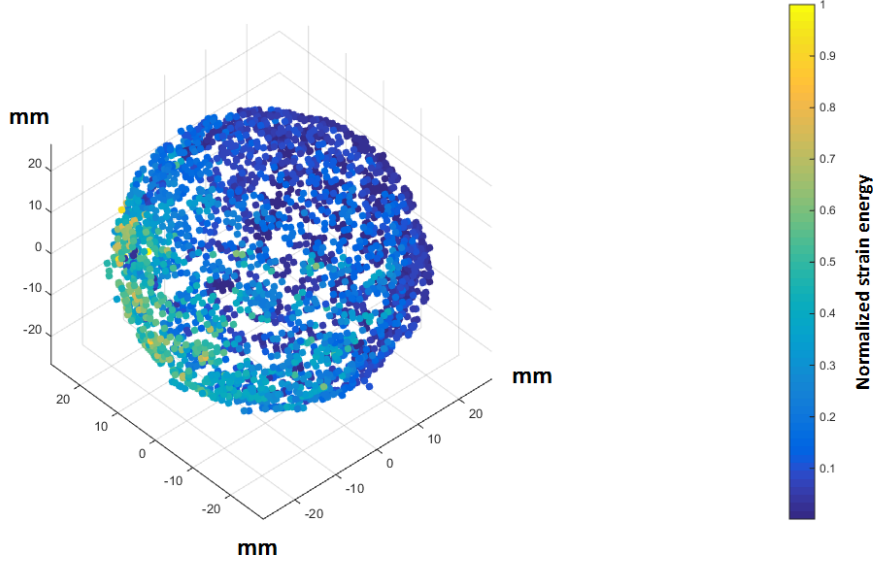
$$p^{inside}(u_i) = F(c_i) \left(\alpha_0 + \alpha_1 \frac{E_i}{E_{max}} \right) \quad (3.8)$$

Where $F(c_i)$ is a cut-off function of TGF concentration as [32]. In our case we considered:

$$F(c_i) = \begin{cases} 1 & \text{inside active layer} \\ 0 & \text{elsewhere} \end{cases}$$

The second part of the multiplication reflects two main effects: a fixed probability with the same value of mitosis in the edge ($\alpha_0 = 0.05$), and another part that depends on the effect of strain component around the wound edge ($\alpha_1 \frac{E_i}{E_{max}}$, where $\alpha_1 = 0.05$, E_i : strain energy component for that area).

Figure 3.8: Example of normalized strain distribution around the wound area, where 0 is the center of the cavity and the values of the axis are in mm



Cell redistribution

Once we have mitosis in the active layer, the new cell will exert hydrostatic pressure on the surrounding cells, leading to a redistribution that has to maintain the equilibrium of the cells at the micro-level. In our case the redistribution has to respect the particular hcp geometry of the lattice, indeed, at the end of the process we need each position to be occupied, at most, by one cell. Similarly to what we do for cell mobility, we create a new state variable $u_i^{mitosis}$, which corresponds to the cells of the active layer that go through mitosis, indeed:

$$u_i^{mitosis} = \begin{cases} 1 & \text{if } n_i < p_i^{inside} \\ 0 & \text{if } n_i > p_i^{inside} \end{cases}$$

Where n_i is randomly generated with uniform probability distribution.

Always similarly to the cell mobility step, we compute a level set after the application of the

diffusion algorithm on the cells that are the results of mitosis ($u_i = 1$) inside the 3D grid. The number of steps for the diffusion has to be larger than the distance of the cell from the edge of the cavity in order to guarantee that it results as a non-zero value inside the cavity (in our case we chose $N_d = D_x/2$), the point with highest value should correspond to the shorter path the cell has to reach the cavity. We consider the redistribution as a succession of cell shifts: if we choose the shorter path we have a minimum number of shifts and a minimum amount of mechanical energy spent. In order to avoid conflicts due to possible equiprobability, we introduce a white noise to the probability value in each position of the cavity.

$$p_i = p_i + 10^{-3}n_i \quad n_i \in [0, 1]$$

The algorithm stops when we reach the same total number of cells of the beginning (Algorithm 3.3)

Algorithm 3.3 Cell redistribution

Application of diffusion algorithm on the matrix which is 1 if cell goes through mitosis, 0 elsewhere.

```

if  $u_i \in \Omega$ 
   $noise = rand \times 0.001$ 
   $p_i = p_i + noise$ 
end if

 $t_A = 0$ 
 $t_B = 1$ 
while  $\sum u_i^{new} \neq \sum u_i^{mitosis}$  do
   $U_0 = \frac{1}{2}(t_A + t_B)$ 
   $u_i^{new} = \begin{cases} 1 & \text{if } p_i \geq U_0 \\ 0 & \text{if } p_i < U_0 \end{cases}$ 
  if  $\sum u_i^{new} > \sum u_i^{mitosis}$  then
     $t_A = U_0$ 
  else
     $t_B = U_0$ 
  end if
end while

```

3.3 Validation of multiscale model

3.3.1 Clinical study

We performed an initial validation of the multiscale model on one subject who resulted eligible for BCT in Houston Methodist Hospital. We designed an official protocol for a pilot study that allowed us to gather different types of data regarding: tumor position and shape, breast surface, visual satisfaction of the patient, and level of pain perceived. We used this information in order to feed the model and validate it with real data. Here below a detailed description of the overall protocol.

Protocol for validation

The protocol name is “A Pilot Study for the Identification of Targets for Clinical Improvement in Breast Conservative Therapy”. All the public information regarding this protocol are available in [15].

The study is a pilot, observational study to record and measure the changes that occur during treatment and healing for BCT in women with non-metastatic breast cancer for comparison to the multiscale model of breast lumpectomy and healing in order to identify targets for improving BCT. The primary objective of the study is the comparison and the possible validation of the multiscale model, whereas secondary objectives are the evaluation of the 3D-SI methods, gathering information related to the use of ultrasound (US) in order to assess changes in lumpectomy position and shape, and describe the course of pain experience by the woman along with the satisfaction with breast cosmesis after BCT, measured with the Visual Analog Scale of Satisfaction (VAS).

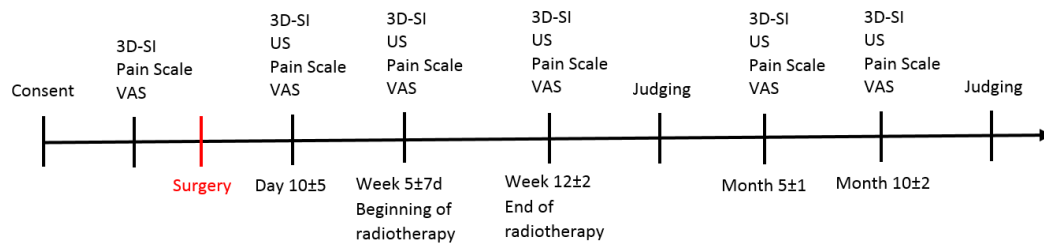
All the subjects have to respect some inclusion criteria:

- Adult females \geq age 30 years
- Have early stage, non-metastatic breast cancer
- Planned to receive BCT

- Have received pre-operative magnetic resonance imaging (MRI) within 30 days before surgery
- Planned to receive post-surgery radiotherapy by whole breast radiotherapy
- Signed informed consent form prior to any research assessment

The study has to follow a specific design consisting of different visits of the patient, before surgery and in specific moments of the healing process (Figure 3.9).

Figure 3.9: Study design



Data from the Operating Room

During the surgery we record different data related to incision orientation, lumpectomy location, tumor position, volume, and weight of the removed tissue. Using a graded cylinder filled by saline solution, we obtain the volume of the tumor mass computing the water displacement from the initial baseline. The same procedure is repeated for all the margins removed from the cavity. The tissue is sent to the pathology laboratory where is measured and weighted. At the end of the procedure of tissue removing, before closing, the cavity is filled by saline and the overall amount of solution is recorded in order to gather additional information related to the volume of the cavity left after tissue removal. At the end of the surgery the surgeon gives information regarding the type of suture and, if there are, comments regarding the tissue, the tumor or the operation itself.

Ultrasound acquisition

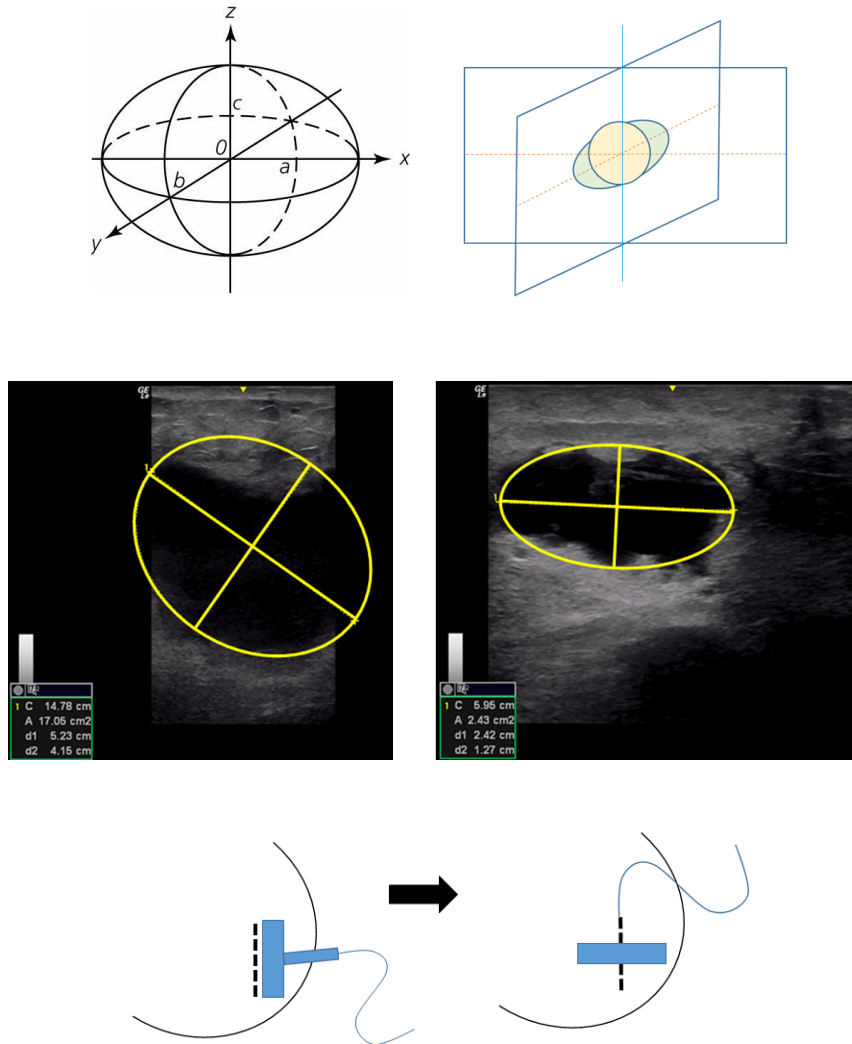
Each post-operative visit of the patient consist of 3D-SI of the breast and US acquisition of the lumpectomy cavity in order to evaluate its position and dimensions. For the US acquisition we used LOGIQe machine by GE Healthcare with the 12L-RS linear probe that has 39 mm field of view and a 5-13 MHz bandwidth (Figure 3.10).

Figure 3.10: Left: LOGIQ e machine. Right: 12L-RS linear probe by GE



We assume the probe to be perpendicular to the skin surface at the moment of the image acquisition and we assume also that the operator who acquires the images selects the image where the cavity results bigger. We acquire two images of the cavity with the probe in perpendicular positions in order to obtain an estimation of the dimensions of the ellipsoid we are approximating the cavity with (Figure 3.11). In this way we can obtain an approximate value of the cavity volume at the moment of the acquisition. Each value of the volume is recorded along with the volume data obtained from the surgery and both are used for the fitting of the multiscale model and its validation. The difference between the volume of tissue removed and the volume obtained by the first US acquisition is used to set the healing speed of the model, whereas the volume values obtained during the following visits are used to evaluate whether the biological model reflects a reasonable physiologic behavior.

Figure 3.11: From the top: ellipsoid that represents the cavity shape and two US acquisitions of the same cavity with probe orientation at the moment of the acquisition



3.3.2 Surface acquisition and comparison

Following the design of the study, we perform 3D-SI of the breast before surgery and in different time steps after surgery. We use the pre-operative acquisitions in order to validate the mechanical model resulting from the segmentation of the MRI data without the effect of the lumpectomy and

the healing process. Post-operative acquisitions, along with US data, are used to monitor the effect of the closure of the cavity on the breast contour and to validate the multiscale model that takes into account the effects of the healing process.

3D-SI is performed using the Kinect system by Microsoft along with Reclution, which is the software that collects the inputs from the Kinect and reconstruct the surface of interest. The clouds of points we obtain are then compared to those obtained from the model and this process is performed using the software CloudCompare [53].

Kinect and Reclution

The Kinect is a recording system by Microsoft (Figure 3.12 on the left) mainly used in gaming industry with size of approximately 30 cm × 7.5 cm × 6.4 cm (w × d × h) and the weight of approximately 1.4 kg. It is a physical device with sensing technology and is made of specific components [45] (Figure 3.12 on the right) :

- An RGB camera (1280×960 resolution)
- An infrared (IR) emitter and an IR depth sensor. The emitter project IR light beams, whereas the sensor reads the beams reflected back by the environment, converting then into depth information
- A multi-array microphone for capturing sound
- A 3-axis accelerometer that determines the current orientation of the kinect.

The device has a viewing angle which is 43° vertical by 57° horizontal, the vertical tilt range is ±27° and the frame rate for both depth and color stream is 30 frames per second (FPS). The accelerometer has a 2G range, where G is the acceleration due to gravity, with a 1° accuracy upper limit.

The IR emitter projects a well defined invisible pattern on the surrounding environment. This pattern is acquired by the IR sensor which, knowing the distance from the source of the emission

and the distance from the specific pattern, performs a triangulation and reconstructs a depth map. Sunlight would destroy the specific pattern, as well as the use of multiple kinects, indeed we used just one device indoor.

The depth map obtained by the kinect is sent to the software Refusion. This software is based on the KinectFusion approach [48] with some modifications: every new cloud point acquired is registered to the current one using an Iterative Closest Point (ICP) Algorithm [7] that solves a problem of minimization between the two entities. In Figure 3.13 we can see the result of the reconstruction of the phantom surface made by Refusion.

Figure 3.12: Top: Kinect device from Microsoft. Bottom: Kinect components

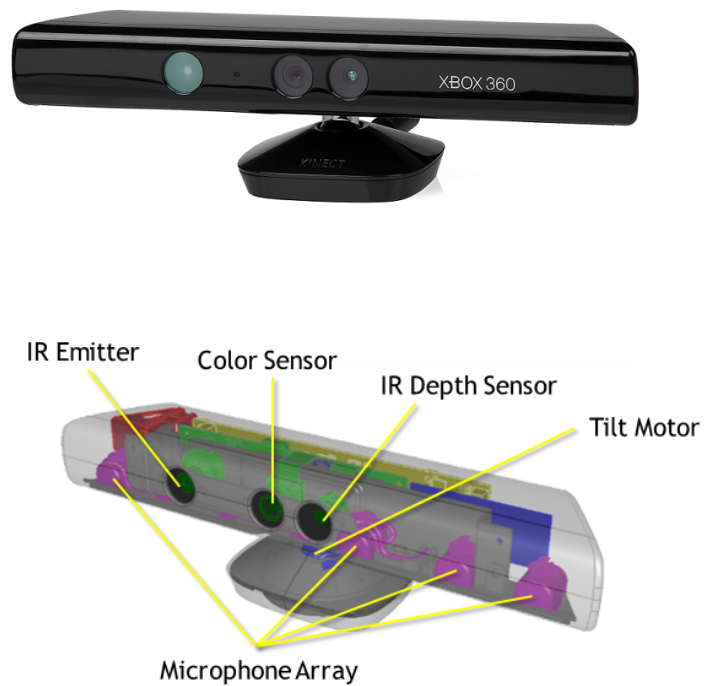
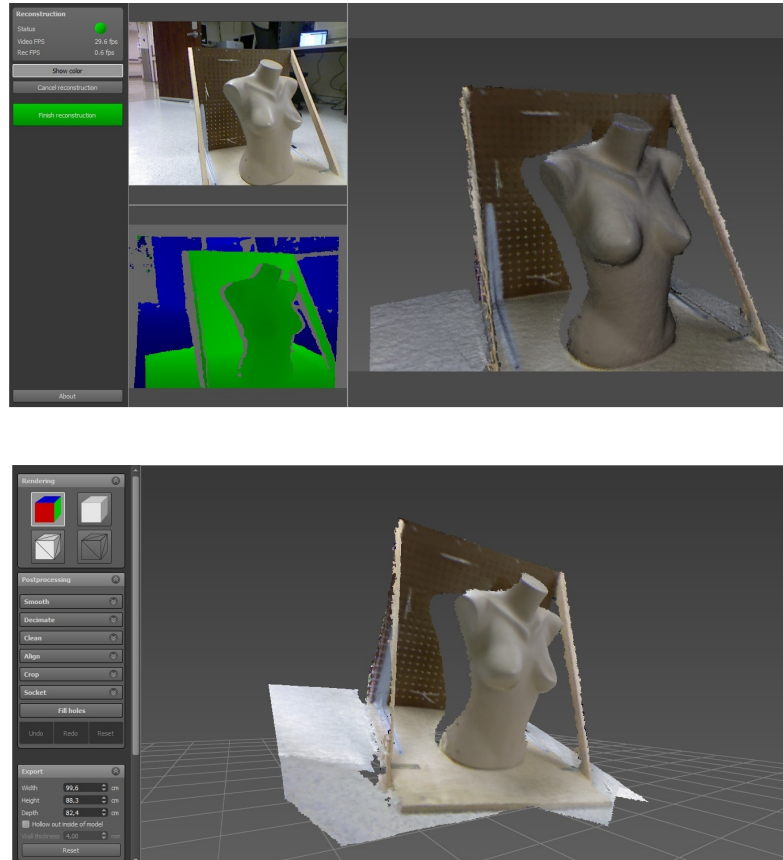


Figure 3.13: Top: Refusion graphic user interface at the moment of the volume acquisition. Bottom: Refusion graphic user interface after the volume acquisition and reconstruction



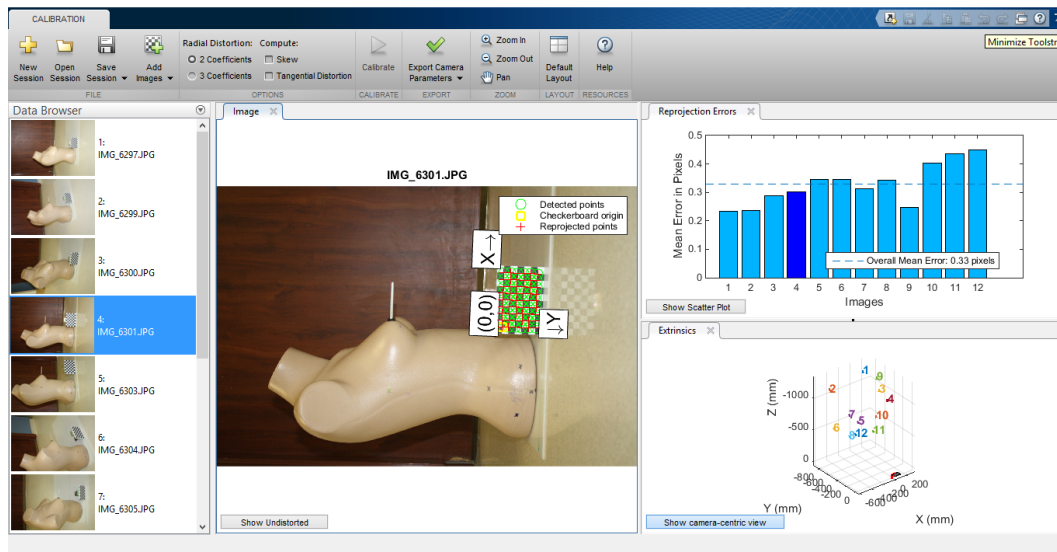
Kinect Validation

In the study made by Henseler et al. [27] the Kinect device was validate for clinical protocols evaluating its accuracy and reproducibility in acquiring breast implants of different volume. The error never exceeded 10% the ground truth volume in all the experiments. We wanted to evaluate again the device performance using a phantom both in static and dynamic conditions (breathing simulation).

We took a profile picture of the phantom and, using the Camera Calibrator app for Matlab (Figure

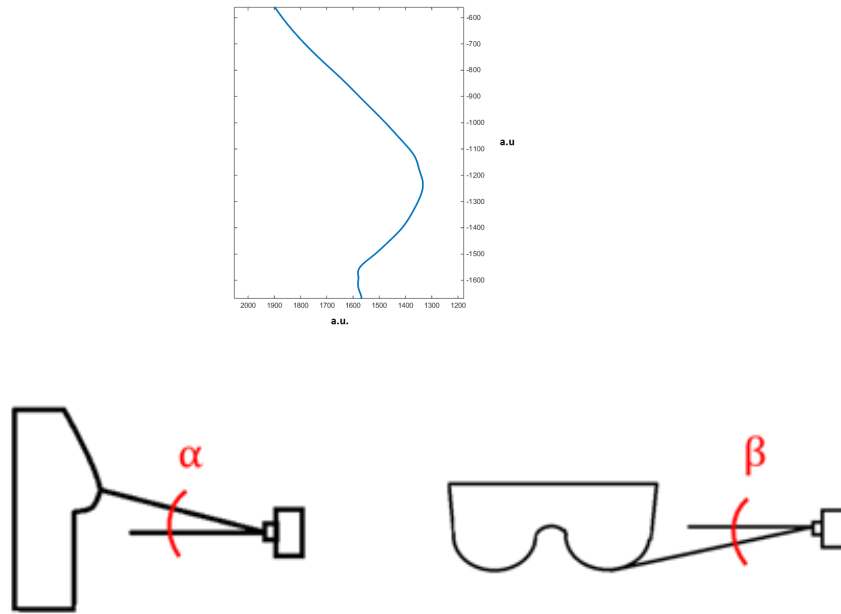
3.14), we could extract the intrinsic and extrinsic parameters of the camera. We had to feed the program with 10 to 20 pictures acquired in different positions of the phantom next to a regular chessboard of well known dimensions, in order to extract the parameters. The software automatically uses the intrinsic parameters in order to correct the image for the lens distortion and the extrinsic parameters to compute the position of the camera in the real space at the moment when the picture was taken.

Figure 3.14: Camera calibrator user interface where we can see: on the left, the list of pictures used to feed the algorithm of calibration, in the center, the result of the chessboard detection, and on the right, the histogram of the mean error for each image and its extrinsic parameters (position of the camera in respect to the chessboard origin which is the top left corner of the chessboard itself).



After this process we could extract the profile of the phantom from the undistorted picture and, after a manual selection of the position of the nipple (that we consider as the reference), we could retrieve the the tilting angles from the camera and the real dimension of the phantom (Figure 3.15).

Figure 3.15: Phantom profile and tilting angles of the camera using the nipple as center of rotation



We proceeded with the surface acquisition of the phantom with the Kinect. In order to obtain a better reconstruction we built a particular support for the device that stabilizes the acquisition and allows a rotational movement around a specific object (Figure 3.16).

Figure 3.16: Support for kinect that allows a rotational movement around the patient breast at the moment of the surface acquisition.



We acquired the surface of the same phantom that we used for the profile extraction. What we needed to do was to orient the resulting cloud point in the same position the phantom was at the moment of the profile extraction, then we could project it, extract its profile, and compare it with the one obtained from the calibration process. We used a box as reference at the moment of the 3D-SI; it gives us the horizontal plane and the plane where was the chessboard at the moment of the profile extraction (Figure 3.17 (a)). After having selected the chessboard plane we selected the area of interest of the phantom, we scaled it in order to obtain the real dimension and we oriented it using the tilting angles obtained from the calibration (Figure 3.17 (b)). For the rotation we applied 3D rotation matrices for all the points. In this way we obtained a cloud of points which represents the surface of the phantom and is oriented in the same position as it was when we extracted the real profile: we could then project the cloud on the x-y plane and obtain its profile. We repeated this procedure several times with different surface acquisitions of the same phantom and we computed the difference between the profile extracted from the calibration and the profile obtain from the point cloud generated by the Kinect.

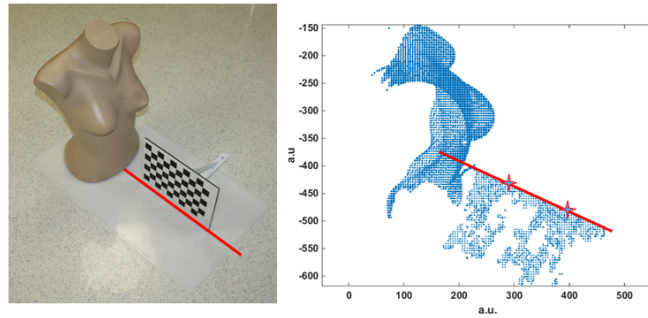
Figure 3.18 shows a qualitative result of the comparison of the two profiles, whereas Figure 3.19 shows the values of the mean error obtained from five acquisitions of the same phantom, both in static and dynamic conditions (breathing simulation).

CloudCompare

CloudCompare [53] is a point-cloud-processing software that relies on an octree structure [35] and it is developed in C++. The cloud point of the breast obtained with the Kinect and the one obtained from the model are both loaded in the workspace of the software (Figure 3.20) where they are registered and compared. The cloud point obtained with the Kinect is first segmented in order to take only the area of interest, then it is scaled in order to match the real dimensions, using the data from the MRI. The two clouds are then registered using a built in function that works with an ICP algorithm [7]. The ICP algorithm needs two clouds that are already roughly aligned and uses one of them as reference while aligns the other cloud to the first one by minimizing the squared errors between the two entities. The algorithm does not need to specify any reference point on the clouds, which is the reason why we chose it: the protocol does not allow us to put any kind of marker on the patient and the breast shape does not show any clear natural reference that could be used. Once the two cloud points are aligned, we could compute the difference between them in terms of distance between the points along the normal of the reference surface.

Figure 3.17: Process of orientation of the cloud point. (a) Reference selection on the cloud point using regular box at the moment of acquisition. (b) Orientation of the cloud point using the nipple as center of rotation and the tilting angles retrieved from the calibration process.

(a)



(b)

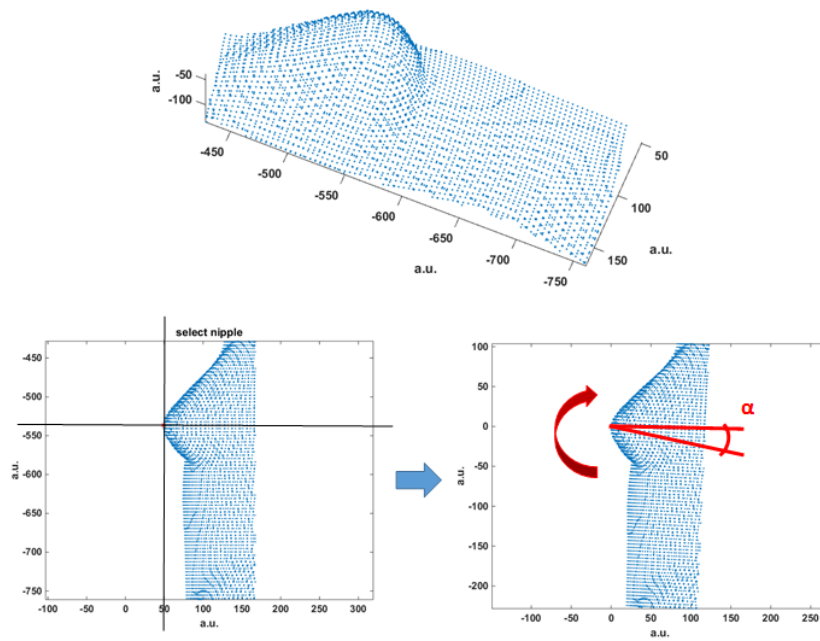


Figure 3.18: Comparison of the 2 profiles

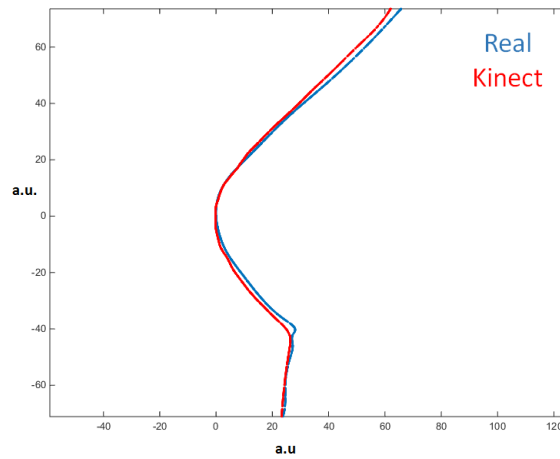


Figure 3.19: errors: left static, right with breathing simulation

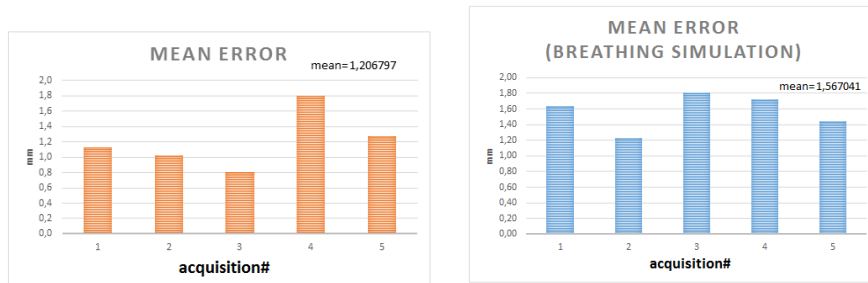
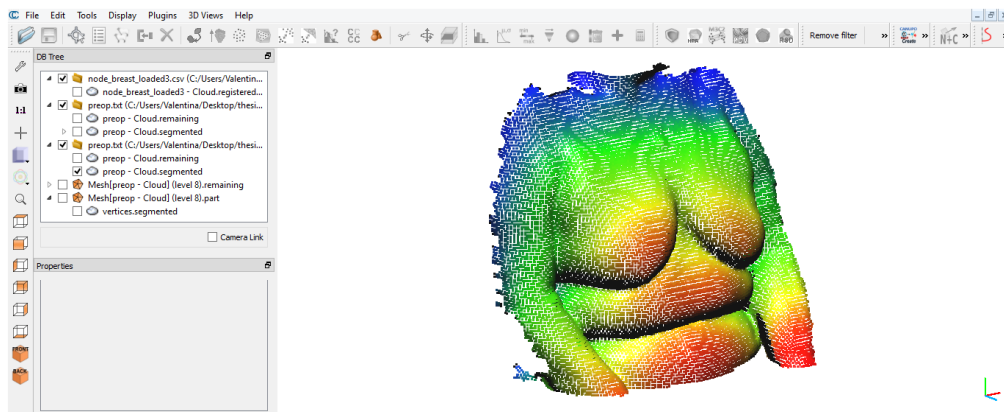


Figure 3.20: CloudCompare workspace where we loaded the result of the 3D-SI of breast



Chapter 4

Results

4.1 Validation of 3D CA

We wanted to assess whether our CA model was behaving as theoretically expected. In order to do that, we tested the model feeding the algorithm with specific stress distributions: in stress free conditions and with a specific pattern of stress. The results shown below are obtained using a volume of dimension (in units) $60 \times 60 \times 60$ with a lumpectomy radius of 20 units.

No-stress condition

We assessed the behavior of the 3D biological model in stress-free condition both to evaluate whether the algorithm is behaving as theoretically expected (no predominant direction of closing), and to obtain an initial simplified model that could mimic particular physiological conditions where we could assume that the stress plays a negligible role. Figure 4.1 shows the healing process of the cavity for the three perpendicular planes that pass by the center of the volume in different moments: right after the virtual lumpectomy (perfect sphere), after 40 time steps and after 85 time steps, where the cavity results almost closed. We can see how the three planes result having different dimensions due

to the nature of the hcp geometry (Equation 3.1). Figure 4.2 (a) shows the symmetric reduction of the diameter of the wound for the three perpendicular planes and Figure 4.2 (b) shows how the center of the cavity does not move significantly from the initial position for all the three planes during the healing process.

Figure 4.1: Evolution of wound closing in stress free conditions for the three perpendicular planes that pass by the center of the volume. From top to bottom: initial condition, after 30 time steps and after 85 time steps.

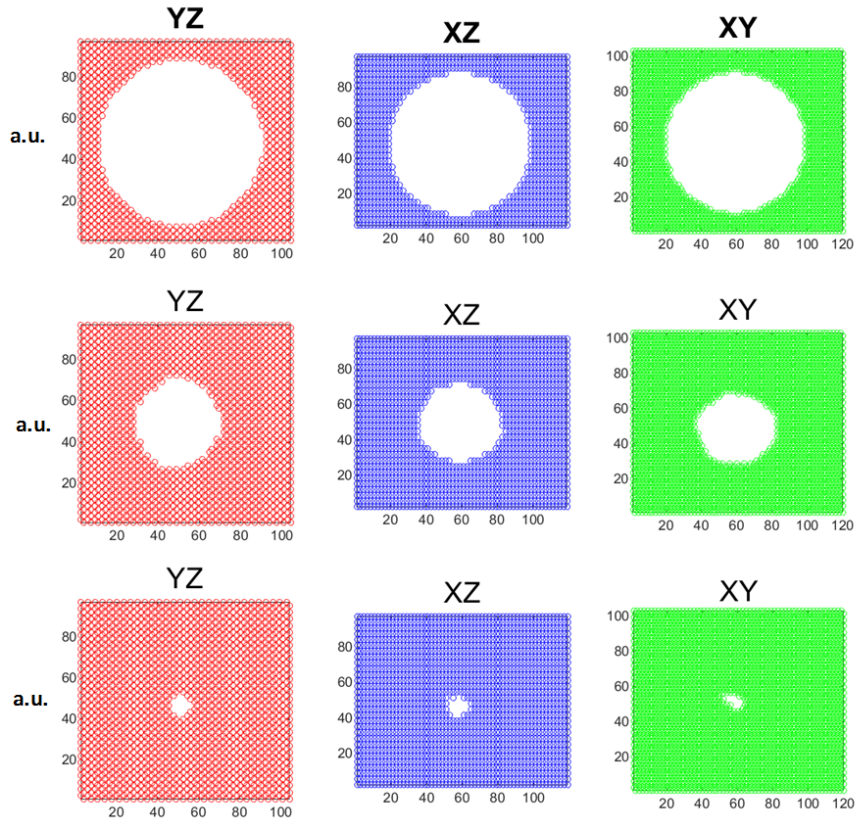
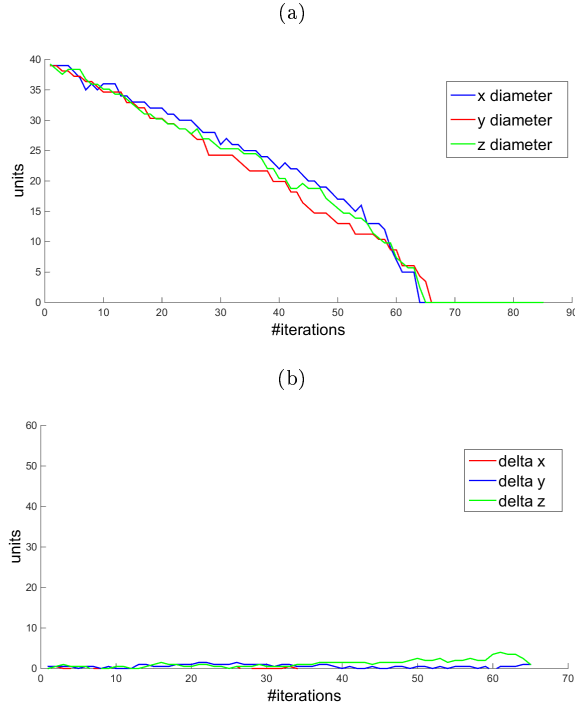


Figure 4.2: a) Diameter (in units) of the cavity for the three different axis passing by the center of the cavity where we can see how the three axis have the same behavior. b) displacement of the center of the cavity from the initial position, where we can see that the center of the cavity does not move consistently from the initial position during the healing process.



Given stress pattern

We fed the model with a specific stress distribution which has the maximum value of stress for half of the overall volume of interest ($z < D_z/2$), whereas the other half has zero level of stress. Figures 4.3 and 4.4 show the results for this configuration.

Figure 4.3: Evolution of wound closing for the three perpendicular planes with maximum stress value for the lower half of the volume and zero for the rest. From top to bottom: after 5 time steps, after 20 time steps and after 55 time steps

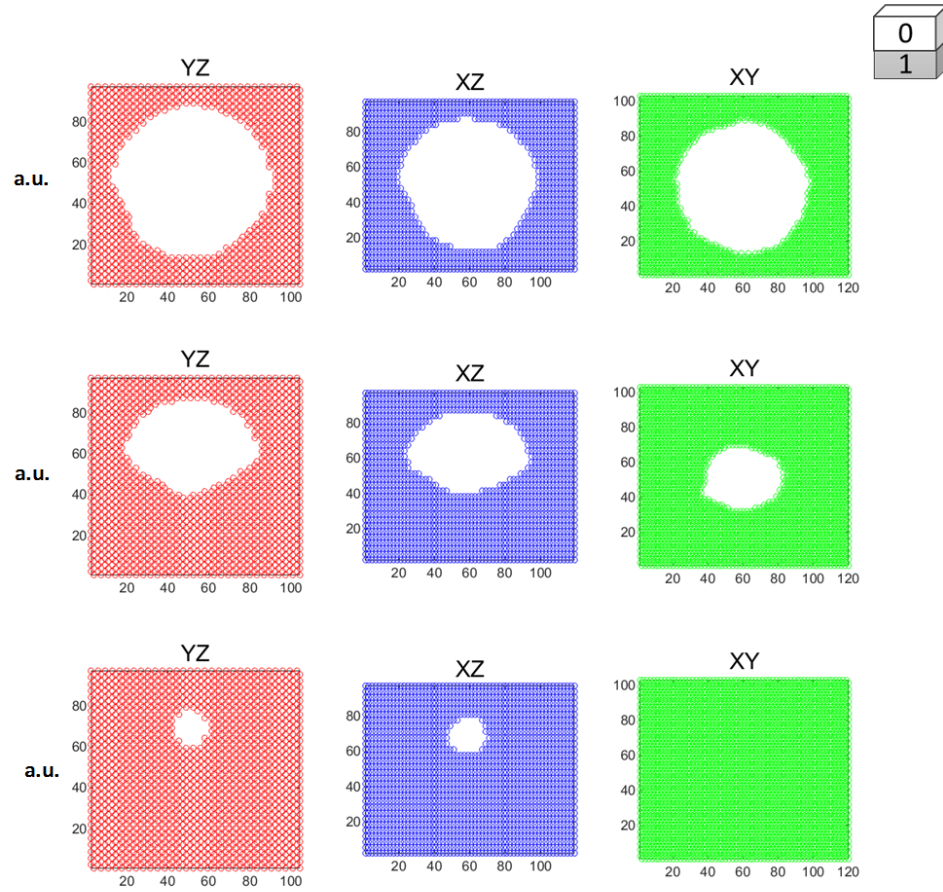
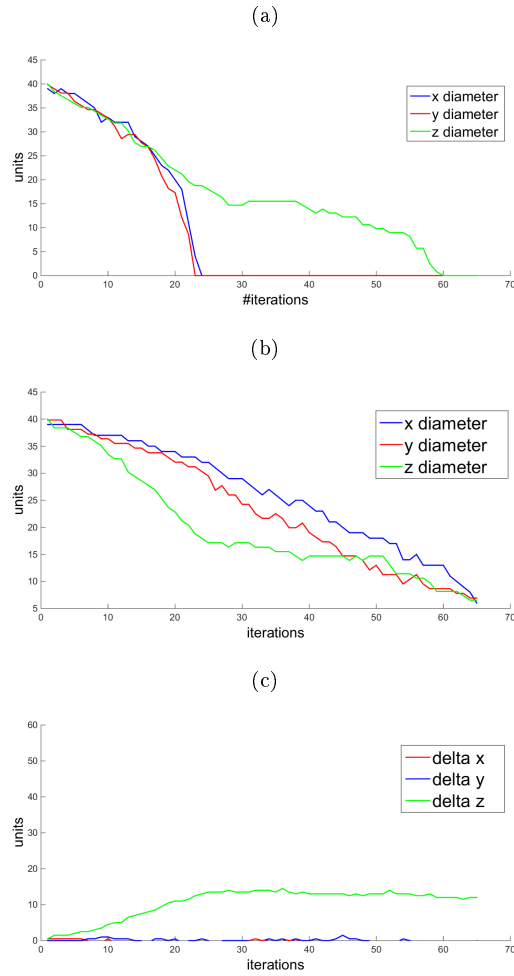


Figure 4.4: (a) Diameters (in units) of the cavity for the three different axis passing by the center of the volume where we can see how the three axis lost the symmetric behavior. (b) Diameters of the cavity for the three different axis passing by the center of the cavity, that changes coordinates for every iteration, as shown in (c) .(c) Displacement of the center of the cavity from the initial position.

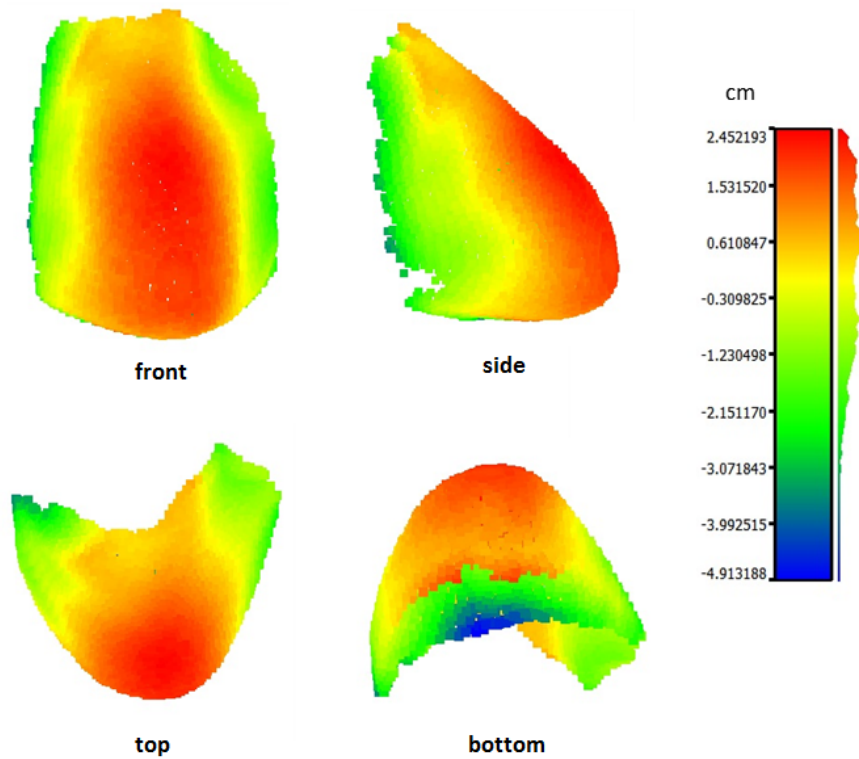


4.2 Validation of the mechanical model

In order to validate the mechanical model of the breast we compared the breast surface obtained feeding the mechanical model with the MRI data of the patient and the breast surface obtained from the pre-operative 3D-SI obtained with the Kinect. The lumpectomy was not performed yet, so

the pre-operative 3D-SI should reflect the shape of the breast at the moment of the MRI acquisition without any possible deformity due to the cavity and the healing process. Figure 4.5 shows the result of this comparison.

Figure 4.5: Results of the comparison between pre-operative 3D-SI and outcome of mechanical model without lumpectomy. The figure shows different views of the breast where the color of each point represents the value of distance (signed) between the model and the reference in cm.

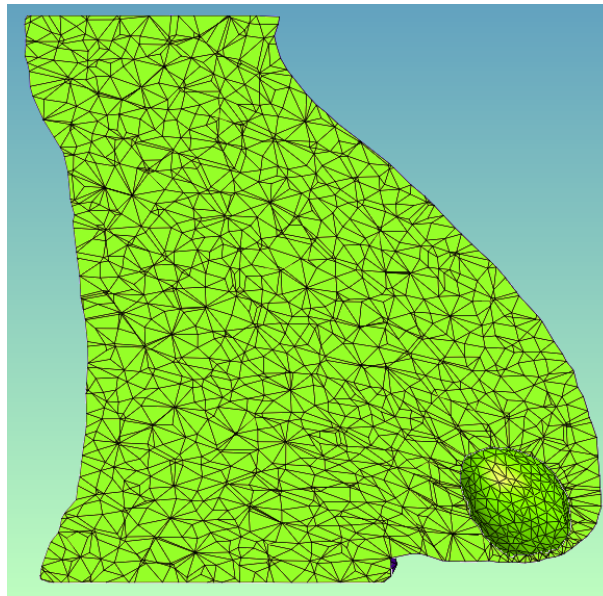


4.3 Rough validation in patient specific case

We performed a virtual lumpectomy on the mechanical model we reconstructed from the MRI of the first patient who took part to the study. The patient had cancer located in the lower inner

quadrant of the right breast. We positioned the tumor as decided by the surgeon during the pre-operative surgery planning, and we initialized it to a sphere. Figure 4.6 shows what we obtained performing a virtual lumpectomy with those characteristics on the reconstructed breast and then applying gravity . The radius of the sphere was set using the data obtained from surgery: the cavity left after surgery had a volume of 65cm^3 , so we set the radius of the virtual cavity to 2.5cm . Figures 4.7, 4.8, and 4.9 show the results obtained from the simulation.

Figure 4.6: Sagittal view of the breast reconstructed from MRI data where we performed a virtual lumpectomy with same characteristics of the patient-specific case, and where then we applied gravity.



From US data obtained during the first and the second acquisition after surgery, we could estimate the volume of the cavity during the healing process as shown in Table 4.1.

Table 4.1: Volume estimation of the cavity during time

| Day after surgery | Volume of the cavity [cm^3] | Radius of the corresponding sphere [cm] |
|-------------------|--|--|
| 0 | 60 | 2.5 |
| 13 | 34.5 | 2 |
| 43 | 8.5 | 1.3 |

Calibrating the healing speed of the model with the first two real values obtained from the patient (0 and 13 days after surgery), we estimated the volume we would obtain for 43 days after surgery;

we obtained a cavity radius of 1.17cm with a correspondent volume of 6.7cm^3 . We have a difference of 1.8cm^3 between model and real values.

We tested the model evaluating the trend of the maximum value of the strain energy during the healing process in two conditions:

1. Cell mitosis does not depend on strain energy ($\alpha_1 = 0$)
2. Cell mitosis depends also on strain energy (as in Equation 3.8)

Figure 4.10 shows the comparison between the two configurations.

Figure 4.7: (a) Initialization of the mechanical model. (b) Result after 30 time steps. (c) Result after 50 time steps.

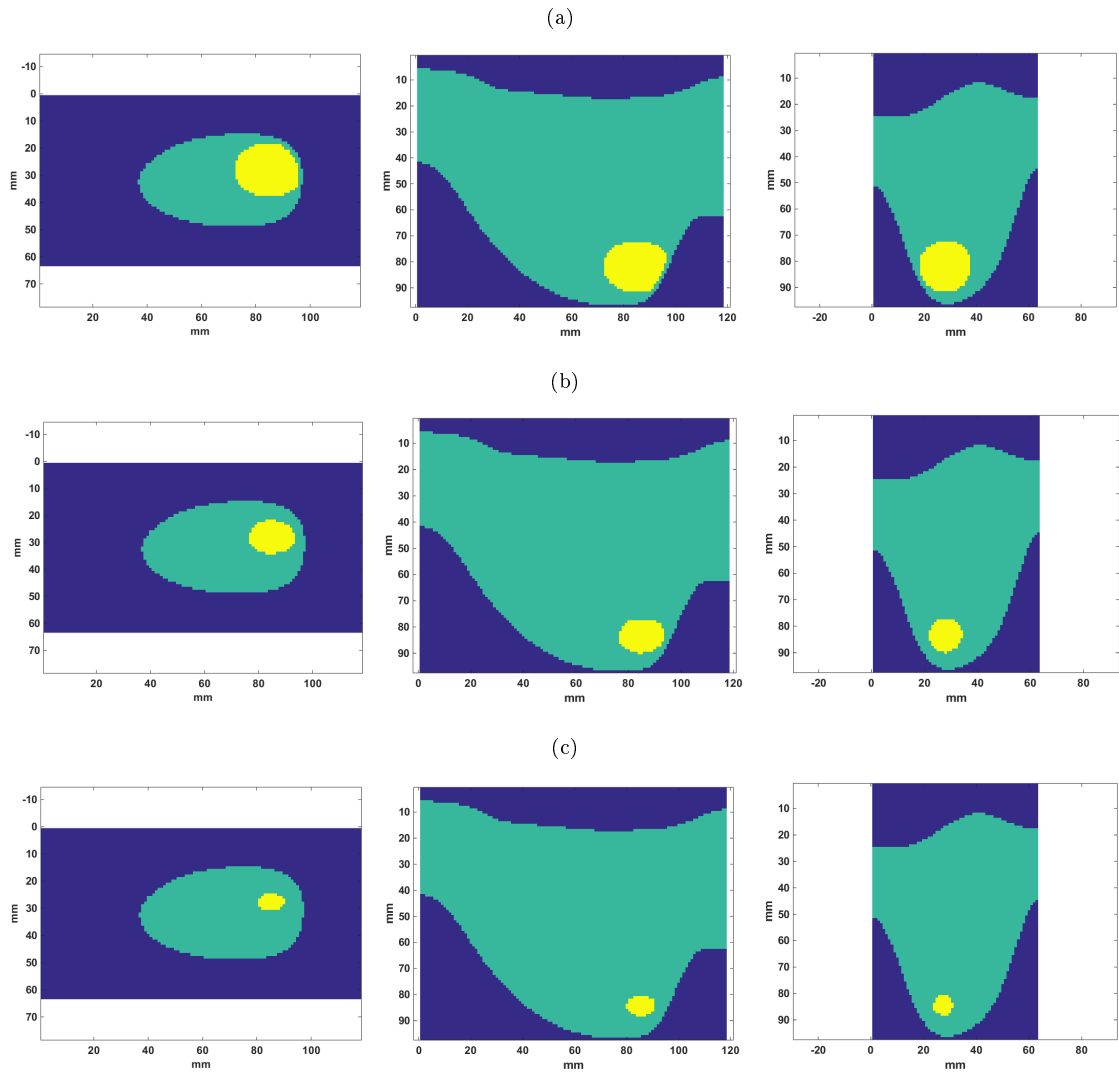


Figure 4.8: Evolution of wound closing from the simulation initialized with real data obtained from the first patient. View for the three perpendicular planes that pass by the center of the volume. From top to bottom: initial condition, after 30 time steps and after 50 time steps

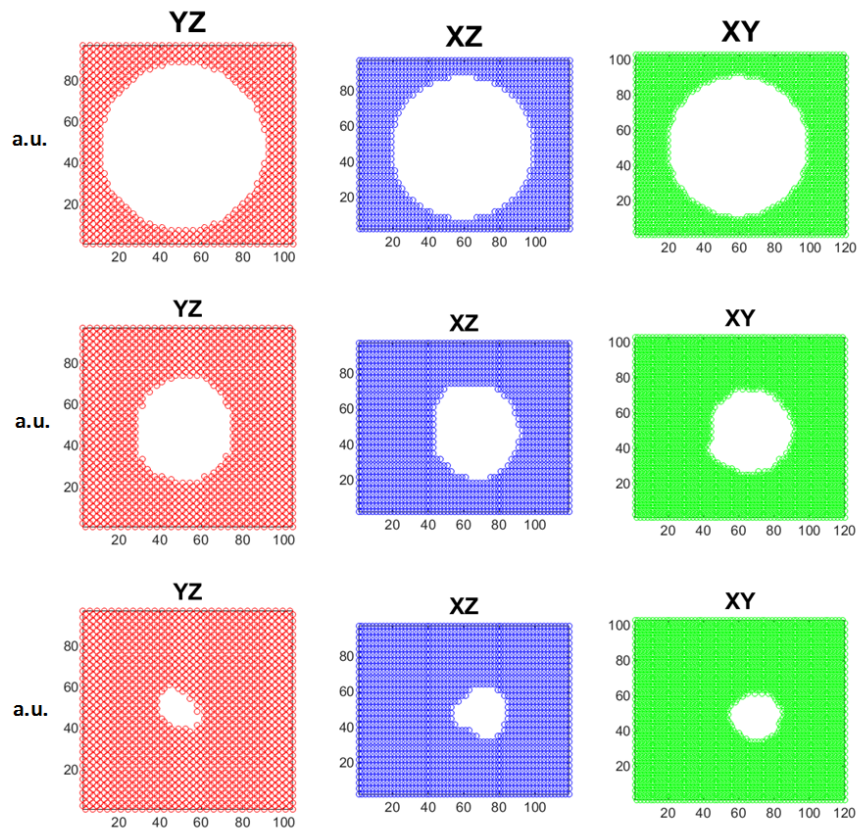


Figure 4.9: (a) Diameters (in units) of the cavity initialized with real values, for the three different axis passing by the center of the volume. (b) Displacement of the center of the cavity from the initial position.

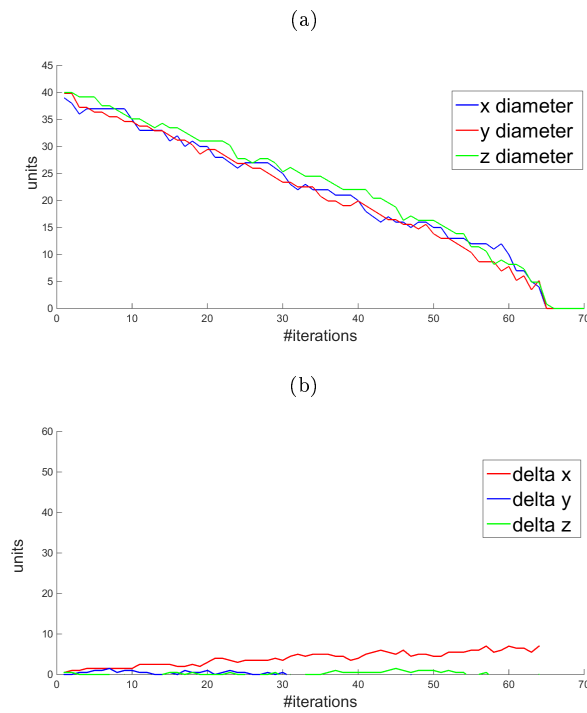
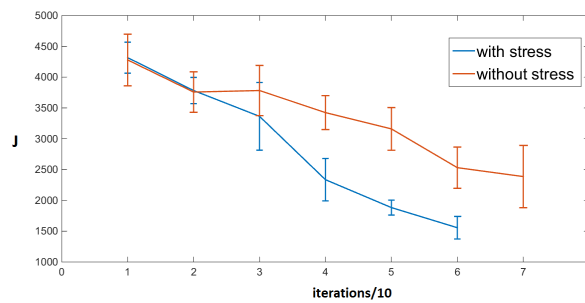


Figure 4.10: Maximum strain energy values (in Joules) during the closing process in two conditions: cell mitosis depends on strain energy (blue), cell mitosis not driven by strain energy (red)



Chapter 5

Discussion and future developments

5.1 Validation of the CA model

The symmetric behavior we can see testing the CA model in stress free conditions (Figure 4.1 and 4.2) proves that the computational framework of the model is working as expected. Considering stress free condition means cancel the effect of stress over the process of mitosis inside the active layer; in Equation 3.8 the value E_i will always have zero value, therefore $\alpha_1 \frac{E_i}{E_{max}}$ will be null in all the points of the active layer and the process of mitosis in the active layer will be driven just by α_0 , resulting in a uniform probability distribution for cell division. The process of healing in this condition will be the result of the combined effects of two uniform probability distributions: cell division at wound edge and cell division inside the active layer without the effect of α_1 . The expected theoretical result has to be symmetric along the three axes with some fluctuations due to the stochastic component of the model. The results we obtained agree with these assumptions. We made the same theoretical approach testing the model with a specific pattern of stress that is maximum for $z < D_z/2$ and zero elsewhere; in this case the effect of $\alpha_1 \frac{E_i}{E_{max}}$ in Equation 3.8 will be maximum for $z < D_z/2$ and null elsewhere, that means, the probability of mitosis for those points that will have the coordinate $z < D_z/2$ will be higher than the others. The direct effect on

the healing process has to be an asymmetry, in terms of closing speed, for the three different axes; this assumption is confirmed by the results shown in Figures 4.3 and 4.4, where we can see how the diameter of the wound along the z axis reduces faster and the position of the center of the cavity moves upward.

5.2 Validation of the mechanical model

The results obtained from the comparison between the surface reconstruct from the mechanical model and the pre-operative 3D-SI show an absolute error that is around the value of 2-3cm. Considering the nature of the surface modifications that we are trying to detect and model, this value is not small. The reasons that explain these results are mainly two:

- The nature of MRI for breast: the acquisition takes place in a particular type of MRI scanner, where the woman is laying face down on a plate that has two circular holes where the breast is positioned in order to be scanned. In case of big breasts, as our case, these holes exert a pressure over the sides of the breast that leads to a deformation. This external compression is not taken into account by the mechanical model and it can be a cause of the error obtained;
- The fact that we are running the simulation attributing average values for the mechanical parameters (Young modulus and Poisson ratio), both for fat tissue and skin. These values influence the final outcome and are patient specific.

In order to overcome these problems we are considering two possible solutions:

- Inverse, in the model, the effect of compression of the breast surface by the MRI scanner during the acquisition.
- Initialize the model with the pre-operative 3D-SI data itself for the breast surface that can be registered with the MRI data.

By doing a registration between the breast surface obtained from the 3D-SI and the MRI data we can solve the problems related to the artifacts due to the nature of the MRI scanner. This should be followed by a calibration of the mechanical parameters using the pre-operative 3D-SI, solving a minimization problem. This calibration will make the model even more patient-specific.

5.3 Rough validation in patient specific case

The tumor was located in the lower inner quadrant of the right breast and during the healing process the cavity experienced higher level of strain energy concentrated mainly in direction of the center of the breast, where probably the breast mass stretches more, due to the effect of gravity. This distribution of strain energy leads to a displacement of the cavity center in the direction of the center of the chest.

The approximation of the volume of the cavity for the 43rd day after surgery fairly agrees with the value obtained from the US data of Table 4.1, but we need more values in order to give a result which is statistically consistent.

The results obtained from the model testing the trend of strain energy values (Figure 4.10) in time, agree with what obtained in [22] for the 2D configuration of the same model: strain energy obtained from the mechanical model shows a relaxation during the healing process if it drives cell mitosis in the active layer. Not considering the effect of strain energy on cell mitosis ($\alpha_1 = 0$ in Eq. 3.8), the trend of the strain energy does not follow a predictable pattern of relaxation.

5.4 Future developments

Algorithm optimization and parallel computing

The 3D multiscale model we implemented is a nice tool, but it needs future improvements in order to be used systematically, mostly because the computational time is long (3 hours for a $60 \times 60 \times 60$

units volume). The system we are modeling is in three dimensions and the biological phenomena that we are mimic require nested **for** loops, whose computational cost becomes consistent when we start dealing with high number of units. In order to overcome this problem, we need a process of algorithm optimization and code translation in a faster coding language, such as C. Along with code optimization, we can significantly reduce the time of computation using techniques of parallel computing, as was done in [22].

3D US reconstruction

The 3D US reconstruction used for this work allow us to have a rough estimation of the volume of the cavity and we could not try other more complex approaches due to the limitations of the protocol: the patient has to sign a specific consent form where there is a specific description of all the procedures that will be performed and all the devices that will be used, and we could not modify easily this protocol. For the future development of the study we will need a more accurate 3D US reconstruction of the volume of the cavity that can give more precise information related to the cavity position in the breast volume and its dimensions in a systematic way, that has to be user friendly at the same time. In order to achieve this goal we could use a system that relies on accelerometers, gyroscopes and magnetometers, that could keep track of the position and orientation of the probe in the space. The machine used for this study had a built-in function for the 3D US reconstruction, but the algorithm behind does not give accurate results, since it does not take into account the speed of movement during the acquisition.

Statistical analysis

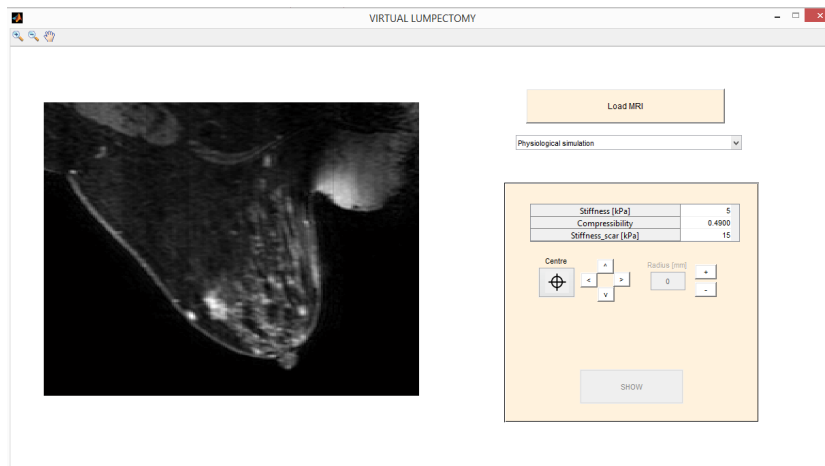
The clinical trial for the validation of the model [15] is still taking place at the Houston Methodist Hospital and plans to gather data from an overall amount of 12 patients eligible for BCT. This collection of information will make possible a statistical analysis which will determine whether the outcome of the model is consistent, or whether it needs further improvements.

Graphic user interface

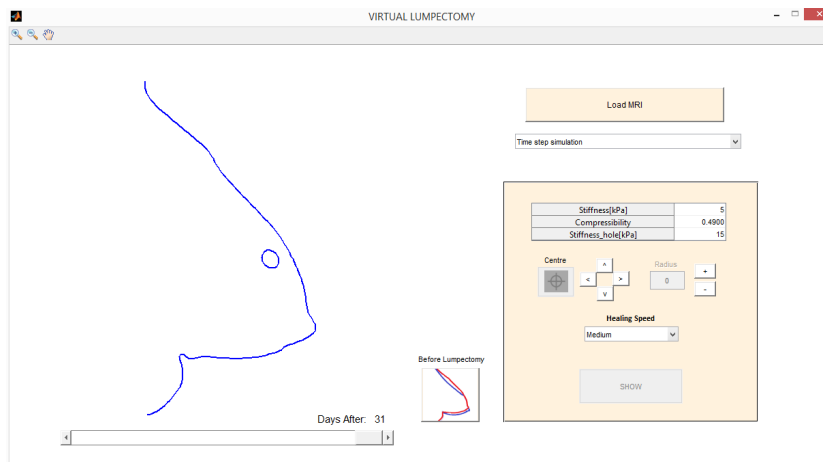
Once the model will give us consistent and robust results, it will need to become systematically usable by surgeons. The idea is to build a software capable of performing a “Virtual Lumpectomy”, where the surgeon loads the MRI data of the patient, and obtain a 3D reconstruction of the breast. The surgeon should be able to change the mechanical parameters of the tissues, along with the position, size, and healing speed of the virtual lumpectomy, and obtain a likely approximation of the final outcome of the surgery. We already developed a prototype of this software for the previous 2D model: Figure 5.1 shows the interface of the software.

Figure 5.1: (a) User interface of the “Virtual Lumpectomy” software, where the user can load the MRI data from the patient files, select the center of the lumpectomy, the radius, and the healing speed. (b) Outcome of the simulation, where the user can see the result of the virtual surgery during the healing process, and obtain an approximation of the time of healing.

(a)



(b)



Bibliography

- [1] S Agarwal, L Pappas, L Neumayer, K Kokeny, and J Agarwal. Effect of breast conservation therapy vs mastectomy on disease-specific survival for early-stage breast cancer. *JAMA Surgery*, 149(3):267–274, 2014.
- [2] G An, Q Mi, J Dutta-Moscato, and Y Vodovotz. Agent-based models in translational systems biology. *Wiley Interdiscip Rev Syst Biol Med. Author manuscript*, 1(2):159–171, 2009.
- [3] Julia Arciero and David Swigon. Equation-based models of wound healing and collective cell migration. In Yoram Vodovotz and Gary An, editors, *Complex Systems and Computational Biology Approaches to Acute Inflammation*, pages 185–207. Springer New York, 2013.
- [4] Julia C Arciero, Qi Mi, Maria F Branca, David J Hackam, and David Swigon. Continuum model of collective cell migration in wound healing and colony expansion. *Biophysical Journal*, 100(3):535–543, 2011.
- [5] Enja J. Bantema-Joppe, Linda de Munck, Otto Visser, Pax H.B. Willemsse, Johannes A. Langendijk, Sabine Siesling, and John H. Maduro. Early-stage young breast cancer patients: Impact of local treatment on survival. *International Journal of Radiation Oncology Biology Physics*, 81(4):e553–e559, 2011.
- [6] LC Barr, AM Brunt, AG Goodman, RH Phillips, and H Ellis. Uncontrolled local recurrence after treatment of breast cancer with breast conservation. *Cancer*, 64(6):1203–7, 1989.
- [7] P.J. Besl and Neil D. McKay. A method for registration of 3-d shapes. *Pattern Analysis and Machine Intelligence, IEEE Transactions on*, 14(2):239–256, Feb 1992.
- [8] A.N. Budrukkar, R. Sarin, S.K. Shrivastava, D.D. Deshpande, and K.A. Dinshaw. Cosmesis, late sequelae and local control after breast-conserving therapy: Influence of type of tumour bed boost and adjuvant chemotherapy. *Clinical Oncology*, 19(8):596 – 603, 2007.
- [9] Svetlana Bunimovich-Mendrazitsky, Vladimir Pisarev, and Eugene Kashdan. Modeling and simulation of a low-grade urinary bladder carcinoma. *Computers in Biology and Medicine*, 58(0):118 – 129, 2015.
- [10] Helen Byrne and Dirk Drasdo. Individual-based and continuum models of growing cell populations: a comparison. *Journal of Mathematical Biology*, 58(4-5):657–687, 2009.
- [11] Li-Hua Chen, Sun-Pui Ng, Winnie Yu, Jie Zhou, and K. W. Frances Wan. A study of breast motion using non-linear dynamic fe analysis. *Ergonomics*, 56(5):868–878, 2013. PMID: 23514244.

- [12] Bastien Chopard, Rafik Ouared, Andreas Deutsch, Haralambos Hatzikirou, and Dieter Wolf-Gladrow. Lattice-gas cellular automaton models for biology: From fluids to cells. *Acta Biotheoretica*, 58(4):329–340, 2010.
- [13] JH Chung, PM Rajagopal, V Nielsen, and MP Nash. A biomechanical model of mammographic compressions. *Biomech Model Mechanobiol.*, 7(1):43–52, 2008.
- [14] RM Clark, RH Wilkinson, PN Miceli, and WD MacDonald. Breast cancer. experiences with conservation therapy. *Am J Clin Oncol.*, 10(6):461–8, 1987.
- [15] clinicaltrials.gov. <https://clinicaltrials.gov/ct2/show/NCT02310711>.
- [16] D Cukjati, R Rebersek, S Karba, and D Miklavcic. Modelling of chronic wound healing dynamics. *Med Biol Eng Comput.*, 38(3):339–47, 2000.
- [17] A. Perez del Palomar, B. Calvo, J. Herrero, J. Lopez, and M. Doblarè. A finite element model to accurately predict real deformations of the breast. *Medical Engineering and Physics*, 30(9):1089–1097.
- [18] Maximilian Eder, Stefan Raith, Jalil Jalali, Alexander Volf, Markus Settles, Hans-G  nther Machens, and Laszlo Kovacs. Comparison of different material models to simulate 3-d breast deformations using finite element analysis. *Annals of Biomedical Engineering*, 42(4):843–857, 2014.
- [19] Cormac Flynn, Andrew Taberner, and Poul Nielsen. Mechanical characterisation of in vivo human skin using a 3d force-sensitive micro-robot and finite element analysis. *Biomechanics and Modeling in Mechanobiology*, 10(1):27–38, 2011.
- [20] P.T. Foteinou, S.E. Calvano, S.F. Lowry, and I.P. Androulakis. Translational potential of systems-based models of inflammation. *Clinical and Translational Science*, 2(1):85–89, 2009.
- [21] National Breast Cancer Foundation. <http://www.nationalbreastcancer.org>.
- [22] M. Garbey, R. Salmon, D. Thanoon, and B.L. Bass. Multiscale modeling and distributed computing to predict cosmesis outcome after a lumpectomy. *Journal of Computational Physics*, 244(0):321 – 335, 2013. Multi-scale Modeling and Simulation of Biological Systems.
- [23] R.T. Greenlee, T. Murray, S. Bolden, and P.A. Wingo. Cancer statistics. *A Cancer Journal for Clinicians*, 2000.
- [24] T. Hales. A proof of the kepler conjecture. *Annals of Mathematics*, 2005.
- [25] Lianghao Han, John H Hipwell, Christine Tanner, Zeike Taylor, Thomy Mertzanidou, Jorge Cardoso, Sebastien Ourselin, and David J Hawkes. Development of patient-specific biomechanical models for predicting large breast deformation. *Physics in Medicine and Biology*, 57(2):455, 2012.
- [26] Haralambos Hatzikirou and Andreas Deutsch. Cellular automata as microscopic models of cell migration in heterogeneous environments. In Stuart A. Newman Santiago Schnell, Philip K. Maini and Timothy J. Newman, editors, *Multiscale Modeling of Developmental Systems*, volume 81 of *Current Topics in Developmental Biology*, pages 401 – 434. Academic Press, 2008.

- [27] Helga Henseler, Alina Kuznetsova, Peter Vogt, and Bodo Rosenhahn. Validation of the kinect device as a new portable imaging system for three-dimensional breast assessment. *Journal of Plastic, Reconstructive & Aesthetic Surgery*, 67(4):483 – 488, 2014.
- [28] Elliot M. Hirsch, Christiana S. U. Chukwu, Zeeshan Butt, Seema A. Khan, and Robert D. Galiano. A pilot assessment of ethnic differences in cosmetic outcomes following breast conservation therapy. *Plastic and Reconstructive Surgery Global Open*, 2(1):–, 2014.
- [29] H. Hoeffelin, D. Jacquemin, V. Defaweux, and J. L. Nizet. A methodological evaluation of volumetric measurement techniques including three-dimensional imaging in breast surgery. *BioMed Research International*, pages 1 – 10, 2014.
- [30] National Cancer Institute. <http://www.cancer.gov/cancertopics/diagnosis-staging/prognosis/tumor-grade-fact-sheet>.
- [31] E. Javierre, P. Moreo, M. Doblara, and J.M. Garcaa-Aznar. Numerical modeling of a mechano-chemical theory for wound contraction analysis. *International Journal of Solids and Structures*, 46(20):3597 – 3606, 2009.
- [32] E. Javierre, F.J. Vermolen, C. Vuik, and S. van der Zwaag. A mathematical analysis of physiological and morphological aspects of wound closure. *Journal of Mathematical Biology*, 59(5):605–630, 2009.
- [33] Fouad Khatyr, Claude Imberdis, Paul Vescovo, Daniel Varchon, and Jean-Michel Lagarde. Model of the viscoelastic behaviour of skin in vivo and study of anisotropy. *Skin Research and Technology*, 10(2):96–103, 2004.
- [34] Laszlo Kovacs, Maximilian Eder, Regina Hollweck, Alexander Zimmermann, Markus Settles, Armin Schneider, Kristian Udovic, Katja Schwenzer-Zimmerer, Nikolaos A. Papadopoulos, and Edgar Biemer. New aspects of breast volume measurement using 3-dimensional surface imaging. *Annals of Plastic Surgery*, 57(6):–, 2006.
- [35] Rensselaer Polytechnic Institute. Image Processing Laboratory and D.J.R. Meagher. *Octree Encoding: a New Technique for the Representation, Manipulation and Display of Arbitrary 3-D Objects by Computer*. 1980.
- [36] R.J. Lapeer, P.D. Gasson, and V. Karri. A hyperelastic finite-element model of human skin for interactive real-time surgical simulation. *Biomedical Engineering, IEEE Transactions on*, 58(4):1013–1022, April 2011.
- [37] Jie Li, Juan Chen, and Robert Kirsner. Pathophysiology of acute wound healing. *Clinics in Dermatology*, 25(1):9 – 18, 2007.
- [38] Chunjun Liu, Kai Ji, Jingjing Sun, and Jie Luan. Does respiration influence breast volumetric change measurement with the three-dimensional scanning technique? *Aesthetic Plastic Surgery*, 38(1):115–119, 2014.
- [39] Brian Mailey, Andrew Freel, Ryan Wong, David T. Pointer, and Kamran Khoobehi. Clinical accuracy and reproducibility of portrait 3d surgical simulation platform in breast augmentation. *Aesthetic Surgery Journal*, 33(1):84–92, 2013.
- [40] S Marino, M El-Kebir, and D Kirschner. A hybrid multi-compartment model of granuloma formation and t cell priming in tuberculosis. *J Theor Biol.*, 280(1):50–62, 2011.

- [41] Torikai H. Matsubara T. An asynchronous recurrent network of cellular automaton-based neurons and its reproduction of spiking neural network activities. *IEEE Trans Neural Netw Learn Syst.*, 2015.
- [42] S McDougall, J Dallon, J Sherratt, and P Maini. Fibroblast migration and collagen deposition during dermal wound healing: mathematical modelling and clinical implications. *Philos Trans A Math Phys Eng Sci*, 364(1843):1385–405, 2006.
- [43] Nathan B. Menke, John W. Cain, Angela Reynolds, David M. Chan, Rebecca A. Segal, Tarynn M. Witten, Danail G. Bonchev, Robert F. Diegelmann, Kevin R. Ward, and The Wound Healing Group Virginia Commonwealth University Reanimation, Engineering Shock Center. An in silico approach to the analysis of acute wound healing. *Wound Repair and Regeneration*, 18(1):105–113, 2010.
- [44] Carsten Mente, Anja Voss-Bahme, and Andreas Deutsch. Analysis of individual cell trajectories in lattice-gas cellular automaton models for migrating cell populations. *Bulletin of Mathematical Biology*, 77(4):660–697, 2015.
- [45] Microsoft.com. <https://msdn.microsoft.com/en-us/library/jj131033.aspx>.
- [46] AD Morris, RD Morris, JF Wilson, J White, S Steinberg, P Okunieff, R Arriagada, M Le, MG Blichert-Toft, and JA van Dongen. Breast-conserving therapy vs mastectomy in early-stage breast cancer: a meta-analysis of 10-year survival. *Cancer J Sci Am*, 3(1):6–12, 1997.
- [47] Hunter R. Moyer, Grant W. Carlson, Toncred M. Styblo, and Albert Losken. Three-dimensional digital evaluation of breast symmetry after breast conservation therapy. *Journal of the American College of Surgeons*, 207(2):227 – 232, 2008.
- [48] Richard A. Newcombe, Shahram Izadi, Otmar Hilliges, David Molyneaux, David Kim, Andrew J. Davison, Pushmeet Kohli, Jamie Shotton, Steve Hodges, and Andrew Fitzgibbon. Kinectfusion: Real-time dense surface mapping and tracking. In *IEEE ISMAR*. IEEE, October 2011.
- [49] Rachel L. O’Connell, Roger J.G. Stevens, Paul A. Harris, and Jennifer E. Rusby. Review of three-dimensional (3d) surface imaging for oncological, reconstructive and aesthetic breast surgery. *The Breast*, 24(0):331–342, 2015.
- [50] Oline Vinter Olesen, Rasmus R. Paulsen, Liselotte Hojgaard, Bjarne Roed, and Rasmus Larsen. Motion tracking in narrow spaces: A structured light approach. In Tianzi Jiang, Nassir Navab, JosienP.W. Pluim, and MaxA. Viergever, editors, *Medical Image Computing and Computer-Assisted Intervention MICCAI 2010*, volume 6363 of *Lecture Notes in Computer Science*, pages 253–260. Springer Berlin Heidelberg, 2010.
- [51] Breast Cancer Organization. <http://www.breastcancer.org>.
- [52] Stanley Osher and James A Sethian. Fronts propagating with curvature-dependent speed: Algorithms based on hamilton-jacobi formulations. *Journal of Computational Physics*, 79(1):12 – 49, 1988.
- [53] Telecom ParisTech. <http://www.cloudcompare.org/>.

- [54] Paolo Patete, Marco Riboldi, MariaFrancesca Spadea, Giuseppe Catanuto, Andrea Spano, Maurizio Nava, and Guido Baroni. Motion compensation in hand-held laser scanning for surface modeling in plastic and reconstructive surgery. *Annals of Biomedical Engineering*, 37(9):1877–1885, 2009.
- [55] Vijay Rajagopal, Angela Lee, Jae-Hoon Chung, Ruth Warren, Ralph P. Highnam, Martyn P. Nash, and Poul M.F. Nielsen. Creating individual-specific biomechanical models of the breast for medical image analysis. *Academic Radiology*, 15(11):1425–1436.
- [56] Remi Salmon, Marc Garbey, Linda W Moore, and Barbara L Bass. Interrogating a multifactorial model of breast conserving therapy with clinical data. *PLoS One*, 10(4), 2015.
- [57] A. Samani, J. Bishop, M.J. Yaffe, and D.B. Plewes. Biomechanical 3-d finite element modeling of the human breast using mri data. *Medical Imaging, IEEE Transactions on*, 20(4):271–279, April 2001.
- [58] Matthew J. Simpson, Alistair Merrifield, Kerry A. Landman, and Barry D. Hughes. Simulating invasion with cellular automata: Connecting cell-scale and population-scale properties. *Phys. Rev. E*, 76:021918, Aug 2007.
- [59] Alexey Solovyev, Qi Mi, Yi-Ting Tzen, David Brienza, and Yoram Vodovotz. Hybrid equation/agent-based model of ischemia-induced hyperemia and pressure ulcer formation predicts greater propensity to ulcerate in subjects with spinal cord injury. *PLoS Computational Biology*, 9(5):e1003070–, April 2013.
- [60] D. Thanoon. *Computational Framework for Local Breast Cancer Treatment*. University of Houston, 2011.
- [61] Chieh-Han John Tzou, Nicole M. Artner, Igor Pona, Alina Hold, Eva Placheta, Walter G. Kropatsch, and Manfred Frey. Comparison of three-dimensional surface-imaging systems. *Journal of Plastic, Reconstructive & Aesthetic Surgery*, 67(4):489 – 497, 2014.
- [62] Frank A. Vicini, Neal S. Goldstein, Helen Pass, and Larry L. Kestin. Use of pathologic factors to assist in establishing adequacy of excision before radiotherapy in patients treated with breast-conserving therapy. *International Journal of Radiation Oncology Biology Physics*, 60(1):86–94.
- [63] Helen V. Waugh and Jonathan A. Sherratt. Macrophage dynamics in diabetic wound healing. *Bulletin of Mathematical Biology*, 68(1):197–207, 2006.
- [64] BJ Wilhelmi, JS Blackwell, SJ Mancoll, and LG Phillips. Creep vs. stretch: a review of the viscoelastic properties of skin. *Annals of Plastic Surgery*, 41(2):215–9, 1998.
- [65] Dieter Wolf-Gladrow. *Lattice-Gas Cellular Automata and Lattice Boltzmann Models - An Introduction*, volume 308. Springer, Berlin, 2000.
- [66] Stephen Wolfram. Cellular automata and complexity: Collected papers.
- [67] Jia Miin Yip, Naila Mouratova, Rebecca M. Jeffery, Daisy E. Veitch, Richard J. Woodman, and Nicola R. Dean. Accurate assessment of breast volume: A study comparing the volumetric gold standard (direct water displacement measurement of mastectomy specimen) with a 3d laser scanning technique. *Annals of Plastic Surgery*, 68(2), 2012.

- [68] Houman Zahedmanesh and Caitriona Lally. A multiscale mechanobiological modelling framework using agent-based models and finite element analysis: application to vascular tissue engineering. *Biomechanics and Modeling in Mechanobiology*, 11(3-4):363–377, 2012.
- [69] Le Zhang, Chaitanya A. Athale, and Thomas S. Deisboeck. Development of a three-dimensional multiscale agent-based tumor model: Simulating gene-protein interaction profiles, cell phenotypes and multicellular patterns in brain cancer. *Journal of Theoretical Biology*, 244(1):96 – 107, 2007.
- [70] Cordelia Ziraldo, Qi Mi, Gary An, and Yoram Vodovotz. Computational modeling of inflammation and wound healing. *Annals of Plastic Surgery*, 2(9):527–537, 2013.